NRL Report 6005

[redacted]

Thermal Shock Evaluation of Refractory Materials as Rocket Nozzle Inserts

E. W. KAMMER AND H. SMITH

Shock and Vibration Branch
Mechanics Division

EUGENE O[illegible]

Atlantic Research Corporation

November 30, 1963

U.S. NAVAL RESEARCH LABORATORY
Washington, D.C.

CONTENTS

Thermal Shock Evaluation of Refractory Materials as Rocket Nozzle Inserts

E. W. KAMMER AND H. SMITH
Shock and Vibration Branch
Mechanics Division

EUGENE OLCOTT
Atlantic Research Corporation

Uninfiltrated sintered tungsten of several densities together with copper or silver infiltrated material used as rocket nozzle inserts were examined using a small scale nozzle but with operational temperature, pressure, and time duration of exposure. The nozzle insert walls were notched in a manner to produce stress raisers and their effects on the fracture patterns established relative ratings for resistance to thermal shock. Room temperature fracture toughness factors were also determined from notched bars of these same materials. This toughness factor served as a quality rating score to order the materials in their ability to resist fracture. It was found that copper infiltrated sintered tungsten rated highest on both the model test and on the fracture toughness scale. Mechanical strain induced in the outer surface of the nozzle insert by temperature gradients across the wall at the beginning of the ignition sequence together with the temperature were measured with the aid of several types of electrical resistance gages. These gages verified that cracking of the nozzle insert wall occurred early in the burning process.

OBJECTIVES

When a complicated device such as the Polaris rocket is developed under conditions of great urgency, it is of first importance that an operational unit be developed that can perform at least according to minimum requirements. In accomplishing this objective it is realized that a more careful and deliberate study of material properties, changes of design, and improvements of the state-of-the-art for material processing will result in improved performance of the missile; therefore, continued research on these subjects is necessary even though an operational unit is available.

This project is concerned with thermal cracking of rocket nozzle liners. The objectives are:

1. To develop an inexpensive test to compare quality of nozzle insert materials from the standpoint of resistance to thermal cracking. The materials studied were basically composed of tungsten, namely, various densities of sintered powders, sintered tungsten infiltrated with silver or copper, and a few forms of high density stock available from several different fabricating processes.

2. To determine the effect of stress raisers for particular nozzle insert configuration in causing thermal cracking of the selected materials. The introduction of artificial flaws in the form could be especially useful in comparing relative quality of the more crack resistant materials.

3. To devise and apply techniques for measuring strain and temperature on the exterior surface of the nozzle insert, thereby establishing the magnitude of strain (or stress) generated by thermal gradients across the nozzle wall. Strain and temperature data as a function of time are helpful in guiding mathematical treatments of this problem.

To accomplish these objectives, a small-scale rocket was used which would subject nozzle insert materials during a static firing to flame temperatures, pressures, and exposure times to approximately full-scale conditions. In one step the nozzle insert material could be disqualified or retained for further consideration. In addition, the relatively inexpensive model permitted economical selection of more nearly isotropic blanks from the fabricators output. Deliberate introduction of controlled flaw geometry to aggravate

*NRL Problem R05-19A; SP Task Nos. 71402 and 71408. This is a final report on this phase of the problem. Work on other phases of the problem is continuing. Manuscript submitted August 1, 1965.

failure in otherwise acceptably crack-resistant compounds thus became meaningful, subject however to the final condition that geometrical scaling to full-size introduces no compromises in material or structural fabrication.

NOZZLE INSERT MODEL

Figure 1 displays the nozzle insert configuration used. Available test fixtures dictated to a great extent the scale and throat opening to be used. The insert was of simple shape so as to facilitate fabrication and contained a smooth cylindrical outer surface on which to mount electrical resistance strain gages of various types. It was first thought that the flange corner radius could be used as a controllable stress raiser. However it soon developed that more severe crack starters were necessary.

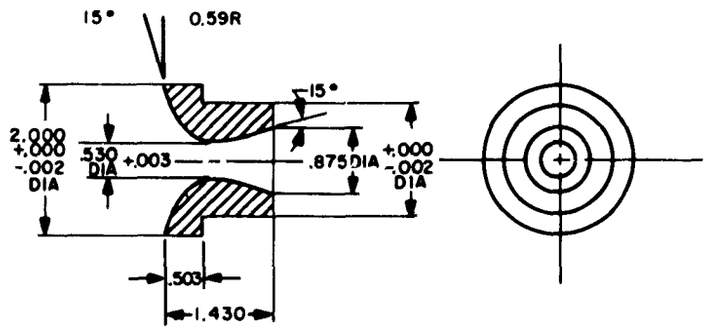

Fig. 1 – Design of nozzle insert

Stress raisers in the form of surface notches were studied in two parallel programs. In one the notches were introduced on the nozzle inserts either with circumferential or axial orientation and their effects on degree of cracking determined after firing. A second program studied the same materials in bar form by measuring the notch bend fracture toughness.

NOZZLE INSERT STRESS-RAISER EXPERIMENTS (ATLANTIC RESEARCH CORPORATION)

Three types of sintered tungsten were considered in this test program; namely, uninfiltrated, silver impregnated, and copper impregnated. The initial sintered matrix ranged from 70 to 90 percent density. Materials from several fabricating companies were compared, and all billets received high-resolution ultrasonic inspection before and after machining. By eliminating material which contained heterogeneities, the interpretation of damage resulting from artificially introduced defects was simplified.

Once the insert geometry had been decided upon, it was essential that the design remain unchanged throughout this phase of comparison testing if the results were to be meaningful. A single exception was made in the first two tests using uninfiltrated 80-percent-dense tungsten inserts on which the sharpness of the flange corner was modified. For one, the radius was 0.10 inch while for the other it was made as sharp as possible with the fabricating techniques available, about 0.002-inch radius.

Except for these two initial tests the effect of stress raisers was examined by introducing notches oriented either in a circumferential direction over the narrowest portion of the throat (Fig. 2) or parallel to the axis (Fig. 3). In the latter orientation more than one notch was usually cut, each having a length of about 3/4 inch and spaced symmetrically about the axis. Various depths up to 0.080 inch were used.

A thread grinding machine with a diamond impregnated wheel served to shape the circumferential notch with an included angle of approximately 60 degrees. The sharpest groove bottom obtainable by this process had a 0.002-inch radius; this profile was able to establish a relative scale which permitted the presently considered

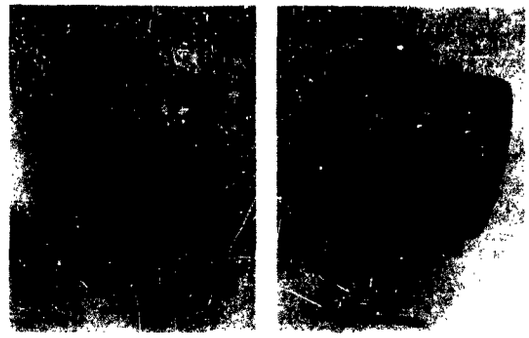

Fig. 2 – Two examples of circumferentially notched nozzle inserts. No thermal cracking occurred in No. 18. A fine crack, entirely along the notch root, was found in No. 17. Both of these models were instrumented with hoop type strain gages which have been melted away during static firing test.

Fig. 4 – Examples of fractures guided by the notches in an uninfiltrated tungsten nozzle insert. Four notch depths ranged from 0.020 to 0.080 inch in equal steps and oriented circumferentially. The two deepest stress raisers guided the fracture path while the shallowest two were ignored. A complete fracture in the axial direction is also obvious.

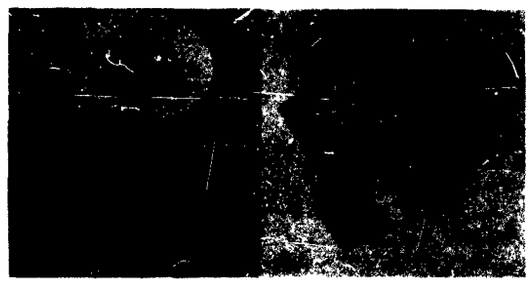

Fig. 3 – An example of fracture induced by a stress raiser of axial orientation in a copper infiltrated tungsten nozzle insert A. The crack location has been emphasized by a dye penetrant coating. The prefiring appearance of this type stress raiser as cut by the Elox process is further displayed by insert B.

materials to be qualitatively rated. For two later trials the circumferential notch was segmented (Fig. 4) into four nicks spaced evenly around the cylindrical surface, the nicks having depths ranging from 0.020 to 0.080 inch in their deepest portions. In this way it was anticipated some bracketing of the optimum depth of notch would become evident. Otherwise the shape of the notch sections was the same as that of the circumferential notches. The notches parallel to the axis were cut by an electric arc process known as Elox. This process results in a more complicated cross section since the removal of material is performed in two steps. A wedge-shaped electrode is first used to excavate the bulk of the notch material, leaving a groove with sides making an angle of approximately 90 degrees at the root. This root is then sharpened with a shim material for the electrode, leaving a slot a few thousands of an inch deep and nearly straight sided. It was capable of generating sharper notch bottoms than the grinder, less than 0.001-inch radius (Fig. 5).

NOTCH BEND FRACTURE TOUGHNESS (NAVAL WEAPONS LABORATORY)

The same materials tested in the nozzle insert configuration were also studied in the form of notched bars. A laboratory measurement at room temperature of the toughness parameter, designated in fracture mechanics (1) by G_c, can also be used to rate these materials from the standpoint of resistance to thermal cracking when stress raisers or flaws are present. This follows from the fact that the maximum stresses causing thermal cracking are generated in the surface at the very beginning of the fuel burning process or while the exterior of the nozzle insert is till at or near room temperature. Under these conditions the toughness parameter determined at room temperature is meaningful in characterizing the potential performance of nozzle materials. In general the greater the value of G_c the more crack resistant is the material.

The bars for the notched bend test were approximately 3/4 × 3/4 × 5 inches in dimension.

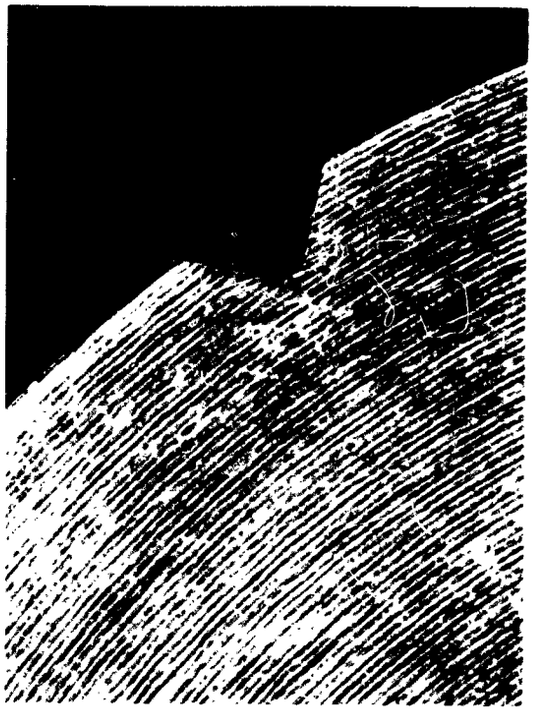

Fig. 5 – Magnified cross-section view of the Elox notch root. The slot in the bottom of the angular notch has a terminating radius of less than 0.001 inch.

A single notch was machined 1/4 inch deep with a 60 degree included angle, the root radius being 0.002 inch or less. This notch was then extended 0.02 inch or more as a fatigue crack developed by flexing the bar in a reverse bending device. During fatigue bending the notch root was exposed to a mildly corrosive solution in order to hasten crack initiation. The solution residue was later removed by washing with solvent, air blasting, and baking the specimen at 225°F for 2 hours.

A four-point loading device was employed both for the fracture force determination as well as for the measurement of specimen spring constant M. This spring constant must be determined for each specimen configuration and material at stress levels well below those which would extend the crack or cause fracture. If the spring-constant parameter is known as a function of crack depth, it is possible to evaluate the derivative contained in an expression of the following form for the toughness factor:

$$G_c = \frac{P^2}{2} \frac{\partial}{\partial a} \left(\frac{1}{M} \right). \qquad (1)$$

Here a is the crack depth and P the load per unit beam thickness. The value of $(\partial/\partial_a)(1/M)$ is best determined in practice by substituting a polynomial expression in powers of a for $1/M$. The coefficients of these power terms are adjusted for best fit to a graph of measured values of $1/M$ as a function of crack depth a. This process is described in detail by Irwin, Kies, and Smith (1).

STRAIN GAGES

Strain measurements were made on the "cold" surface of the nozzle insert to determine the magnitude of the distortion caused by the large temperature gradient which exists across the nozzle insert wall shortly after the motor fuel is ignited. Three types of electrical resistance strain gages were employed. The first, a strippable foil gage, was bonded with ceramic cement and was oriented to measure strain in the axial direction (Fig. 6A). To attach this gage on the nozzle insert wall a ceramic cement is first applied in a thin coat to the clean metal surface. This cement is fired at a relatively low temperature of about 600°F. The strippable foil element with leads attached is then applied to the coated surface, covered with the same ceramic slurry, and again the unit is fired at 600°F.

A second strain gage type (Fig. 6B), a weldable fixture, has a foil resistance element cemented to a flexible metal base which is about 0.005 inches thick. The exposed edges of this base permit the gage to be spot-welded or seam-welded into the desired position on a structure; the strain being transmitted through the welds to the base and thence through the cement to the foil. The great advantage of this type gage is simplicity of installation. In exchange for this convenience some sacrifice is made in the fidelity of the strain reading through the devious linkage path between foil and structure. Vibrations of the flexible base similar to an edge-clamped diaphragm can complicate the output signal by being superimposed upon the structure distortion as seen by the resistance foil element. This type strain gage is also less intimately coupled thermally to the strained structure and some evidence of this lag in following the temperature of the insert surface will

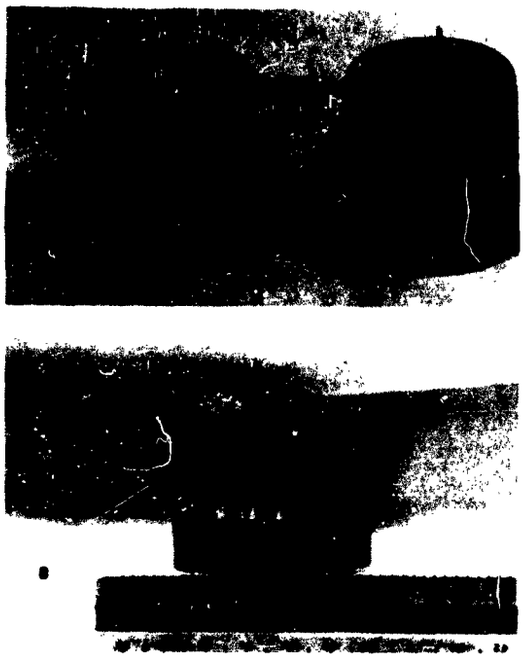

Fig. 6 — Welded strain gages (A) attached to a nozzle insert ready for connection to external circuitry and mounting into adaptor coupling on fuel case. Strippable foil transfer strain gages (B) cemented to a nozzle insert ready for connection into external circuitry.

be pointed out in the records obtained. Nevertheless, this is a useful form of the electrical resistance strain gage for applications to moderately high temperatures. The particular type of gage used for this program was not sufficiently flexible to conform to the curvature of the nozzle exterior for circumferential strain reading but performed acceptably in the axial direction.

The third form, a "hoop" or circumferential gage was made by winding 0.001-inch-diameter constantan wire around the insert subsequent to having coated and fired the surface with a thin ceramic film as was done for the strippable type. After the lead terminals were anchored, an additional coating of the same ceramic slurry was applied over the winding. This was followed by firing to complete the gage attachment. Ribbon leads of constantan were welded to the gage terminals to make connection to the external circuit.

The resistance change of the gage element of a strain gage may be considered to be composed of three components: (a) that caused by a strain which is a result of stress, (b) that caused by a strain which is the difference between the coefficients of expansions of the base and the gage element multiplied by the temperature change, and (c) that equal to the temperature coefficient of resistance of the gage element times the temperature change. This is expressed mathematically

$$\left.\frac{\Delta R}{R}\right|_{total} = \left.\frac{\Delta R}{R}\right|_{stress} + G(\alpha_b - \alpha_g)\,\Delta T + \beta \Delta T \qquad (2)$$

where R is the resistance of the gage element and G is a constant (generally called the gage factor) by which one multiples the strain of a gage element in order to determine the per unit resistance change of the gage element. The linear coefficients of temperature expansion are given as α_b and α_g for the base material and gage material respectively, and β is the temperature coefficient of resistance of the gage element. If Eq. (2) is divided by G it will be converted into units of strain. Thus the component of strain caused by stress is equal to

$$\epsilon_\sigma = \left.\frac{\Delta R}{GR}\right|_{total} + \left(\alpha_g - \alpha_b - \frac{\beta}{G}\right)\Delta T \qquad (3)$$

$$= \frac{\Delta R}{GR} + \left(\alpha_g - \alpha_b - \frac{\beta}{G}\right)\Delta T. \qquad (4)$$

The term $\Delta R/R$ in Eq. 4 is the measured per unit change of resistance of the strain gage.

For all metals, except those especially alloyed to have very small temperature resistance coefficients, the factor β/G is more than an order of magnitude greater than the factor $(\alpha_b - \alpha_g)$. However for those special alloys such as constantan, advance, cupron, and evanohm, these two factors are of about the same value. By carefully controlling the heat treatment of these alloys these two factors can be made nearly identical. When this is done the term $(\alpha_g - \alpha_b - B/G)$ in the last equation vanishes and the gage becomes independent of temperature changes. This is the principle involved for most temperature compensated gages. As these factors are not independent of the temperature the compensation will hold for only a temperature range of about several hundred degrees before errors become excessive.

Table 1 gives typical values for these factors for some materials of concern. The first three materials shown in the table may have their temperature coefficients of resistance vary within the ranges shown, and in the room-temperature region they can be adjusted to specific values by special heat treatments.

actual firing, the temperature of the surface on which the strain gage is mounted is measured by means of a thermocouple. Any strain induced in the "cold" surface beneath the strain gage caused by thermally induced stresses can then by determined by subtracting the isothermal strain value given on the curve (Fig. 7), obtained during the

TABLE 1
Temperature Coefficients of Resistance and Expansion, and Resistivity – Strain Coefficient (Strain Gage Sensitivity Factor) for Some Selected Materials

Material	Temperature Coefficients Resistance × 10^{-6}*	Temperature Coefficients Expansion × 10^{-6}*	Gage Factor
Constantan (Advance)	8 to 30	15.0	2.1
Cupron	− 20 to + 20	14.9	2
Evanohm	− 20 to + 20	14.0	2
Iron	5000	11.7	4
Steel (piano wire)	3000	12	3.7
Invar	2000	0.8	
Molybdenum	3300	5.0	
Tungsten	4500	4.0	

*Per degree centigrade.

Thermal effects on the strain gage response such as the above will be indescriminately represented as nozzle deformation in the output signal. In order to extend the time interval after ignition during which useful information can be retrieved from the strain gage output, these thermal effects must be taken into account. This was accomplished by putting each insert complete with strain gages in place through several heating cycles. The apparent strain read by the gage as the assembly was slowly heated provided a correction curve from which values could be taken at any temperature. By performing this cycle slowly enough, essentially isothermal condition is achieved free of gradients. Such a strain gage temperature correction curve is shown in Fig. 7. In this case there is no stress. When a strain gage reading is obtained for an unknown stress condition and for a known temperature, it is only necessary to subtract the strain gage temperature correction factor to obtain the strain caused by stress. In an

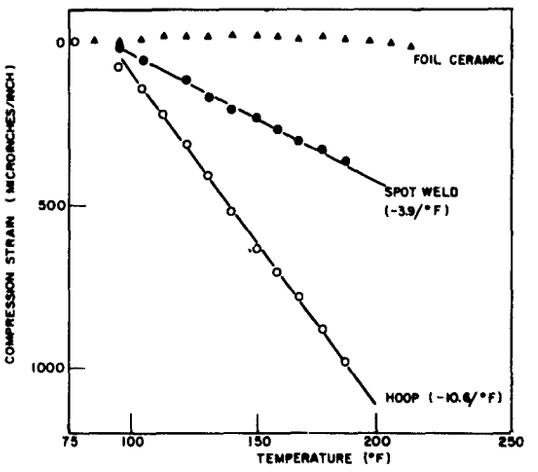

Fig. 7 – Examples of strain gage temperature correction curves for the three types of installations employed in this program, namely, the foil (strippable) ceramic, the weldable unit, and the wire wound (hoop) gages

preheat cycle for the value corresponding to the measured surface temperature, from the measured value of apparent strain.

Temperature measurements were obtained from chromel-alumel thermocouples. For several initial firings, the junction of the couple was pushed against the insert surface through an access hole in the mounting assembly insulation and case. It was hoped that the pressure contact would give adequate thermal coupling. Experience in later trials proved that spot welding the wires composing the couple directly to the tungsten insert was permissible. In no instance could a crack origin be attributed to a surface flaw introduced by this attachment. Furthermore, reproducibility of the temperature readings improved markedly and higher temperature values were indicated than those read by the pressure contact mounting. Figure 8 is a plot of five thermocouple records installed on a single nozzle insert. The couples were mounted around the circumference but in the same cross section plane, so that all should sense very nearly the same temperature. Two of the couples (Nos. 1 and 5) were pressure mounted, while Nos. 2, 3, and 4 were spot-welded to the tungsten. Couple No. 5 was composed of a tungsten/tungsten molybdenum alloy in order to extend the maximum readable temperature range. Acquisition of accurate temperature information is important in order that proper corrections to the measured strain data can be made.

The alloy used for the conductor in the strippable foil type can be conditioned by heat treatment to be independent of temperature over several hundred degrees if the structure upon which it is mounted has an expansion coefficient within the range from about 3ppm/°F to 12 ppm /°F. This spread includes the expansion coefficient for tungsten, which is nominally 3ppm/°F. The manufacturer can select the alloy on a batch basis from which to fabricate the gage grids and thus market units having expansion coefficients close to the single advertised value. In spite of this fairly close match, the spread in expansion coefficient (Figs. 9-11) for the forms of tungsten and infiltrates used in this program necessitated individual calibration of each installation. Several cycles up to about 300°F helped to stabilize the foil-ceramic complex and linearize the resistance vs temperature relationship. These precautions were found to be important if meaningful data were to be retrieved from these and the other types of gages used in this test.

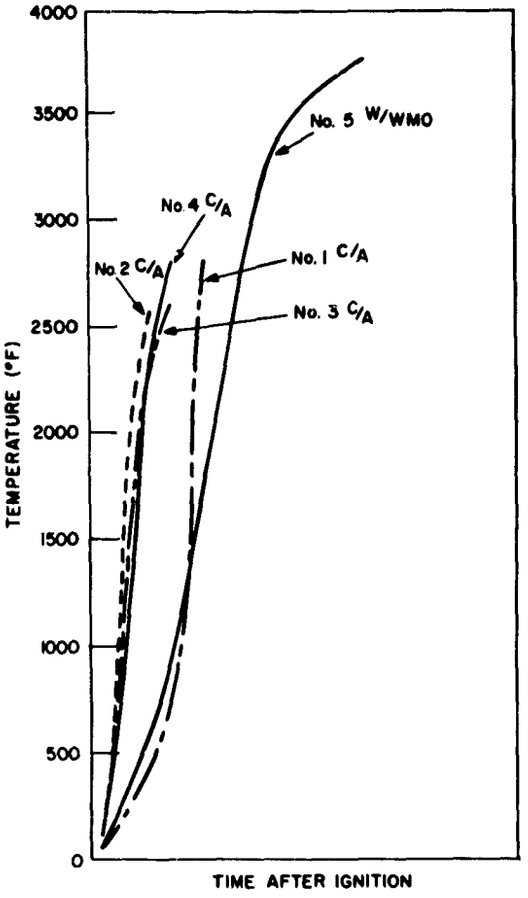

Fig. 8 — A comparison of surface temperature readings for two methods of thermocouple attachment. Traces labeled Nos. 5 and 1 were obtained from junctions pressed against the tungsten insert surface. Junctions yielding traces Nos. 2, 3, and 4 were formed by spot welding the individual wires to the insert surface. The couples were composed of chromel/alumel except for trace No. 5 which was formed from tungsten/tungsten molybdenum alloy in order to extend the maximum readable temperature somewhat. The time scale was omitted because of the indeterminacy of the zero value in some cases.

A few comments may be made regarding the magnitude of the strain correction required for the various types of gages due to their being subjected to a rapidly increasing temperature during measurement. As already stated the conducting material in the strippable transfer gage

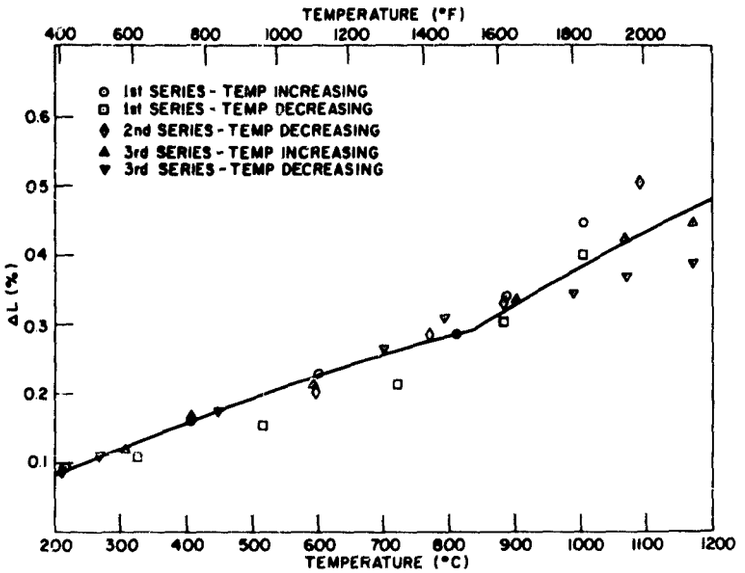

Fig. 9 – Thermal expansion of sintered 75%-dense uninfiltrated tungsten

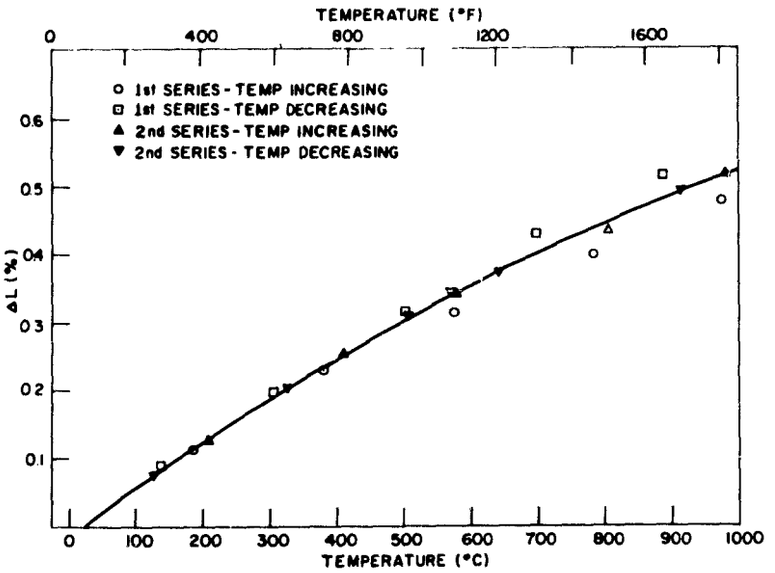

Fig. 10 – Thermal expansion of sintered 80%-dense tungsten infiltrated with silver

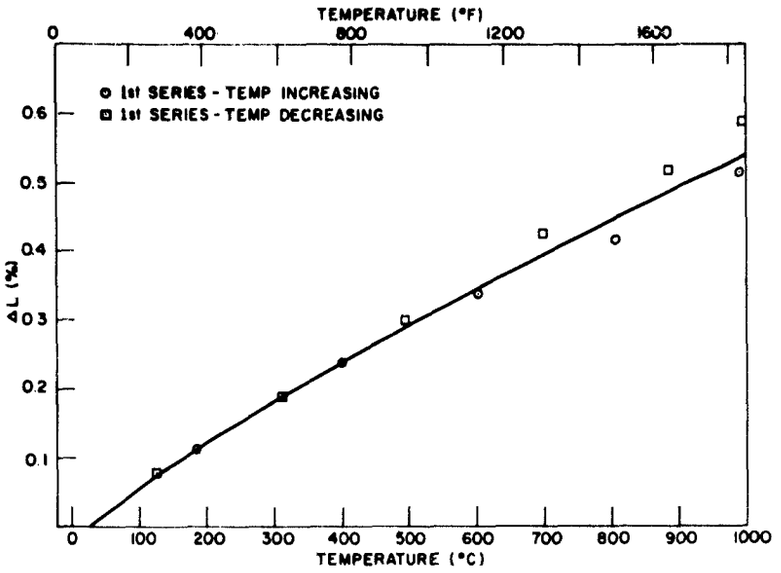

Fig. 11 — Thermal expansion of sintered 80%-dense tungsten infiltrated with copper

is annealed so that temperature independence is achieved over a small temperature range (several hundred degrees) when applied to tungsten. The graphs of change in resistance, derived from prefiring heating cycles such as shown on Fig. 7 were essentially linear relationships. The slope of this line for these gages was less than 1 microinch per inch per degree Fahrenheit and often close enough to zero to be negligible.

No deliberate prefabrication temperature-compensating anneal had been performed for the one-mil-wire conductor comprising the hoop gage. Consequently a large slope for the resistance versus temperature graph is to be expected. This slope averaged close of 10 microinches per inch per degree Fahrenheit and was negative. Furthermore it is important to cycle an installation using unannealed resistance wire at least up to the maximum temperature forwhich it will be useful in order to avoid structural modification of the alloy taking place simultaneously with the measurement of strain and to otherwise stabilize the installation.

The situation presented by the weldable gage is more complex since an intermediate metal is transferring the deformation information to the sensing foil conductor. This coupling metal has a larger coefficient of expansion than the tungsten but is constrained by the welded periphery. For large increases in temperature, buckling by compression of this gage base is to be expected. The moderate increases in temperature during the useful reading time of this test revealed no such discontinuity in performance. Again the slope of the resistance-temperature correction curve was negative and had a value ranging from 3 to 4 microinches per inch per degree Fahrenheit.

Finally, the list of anticipated corrections to the observed strain signal should include some estimate of the surface distortion caused by pressurization of the nozzle insert considering it as a thick walled cylinder. Although the only pressure measurement made was in the fuel burning chamber, this value when used with the dimensions and elastic properties of the insert material can set a maximum bound for the effect of pressure on the strain readout. At the outer surface, where the strain measurements were actually made, this upper bound of tangential stress (2) is given by

$$\sigma_t = \frac{2PR_1^2}{R_2^2 - R_1^2} \tag{5}$$

where R_1 and R_2 are the inner and outer radii for the wall respectively and P is the internal pressure.

Assuming a value for Young's modulus of 50 $\times 10^6$ pounds per square inch and an exhaust pressure of 500 pounds per square inch, the above formula applied to the throat dimensions of the nozzle insert yields a maximum strain of about 3 microinches per inch. The detection of a strain of this magnitude for this type of tests would be difficult. Hence, any contribution to the output signal from the strain gages due to pressurization has been neglected.

THERMAL EXPANSION AND CONDUCTIVITY

Measurements were made of the thermal expansion for three typical densities of sintered and impregnated sintered tungsten (3). The results are included in Figs. 9-11. These samples were in the form of cylinders 2 inches in length and 1-5/8 inches in diameter furnished from the same production batch supplying the nozzle insert blanks.

Thermal conductivity was also determined for these cylinders (Figs. 12-14). The curves on Figs. 12-14 show a significantly lower conductivity for unimpregnated tungsten than the samples infiltrated with copper or silver. It is probably not significant that copper impregnated tungsten is shown to be a somewhat better conductor than the same density silver impregnated material. Heterogeneity of infiltration was apparent from ultrasonic inspection and could account for this unlikely situation.

THERMALLY INDUCED FRACTURES

Thermal Environment

Each static firing lasted 30 seconds and was performed with Aerocel 163 motor fuel which under an equilibrium pressure of 1000 psi supports a flame temperature of about 6500°F. A typical analysis of exhaust gas composition flowing over the insert is in Table 2. Uninfiltrated nozzle liners of sintered tungsten readily absorb the molten Al_2O_3 present in the jet. This process and its possible effects on the insert performance is discussed in the appendixes A, B, and C.

Fracture Patterns

The relative resistance of materials of poor quality to the thermal environment of rocket nozzles can be determined by comparing the fracture pattern induced by the test. It is assumed that the more extensive and penetrating the fracture pattern, the worse the material; however,

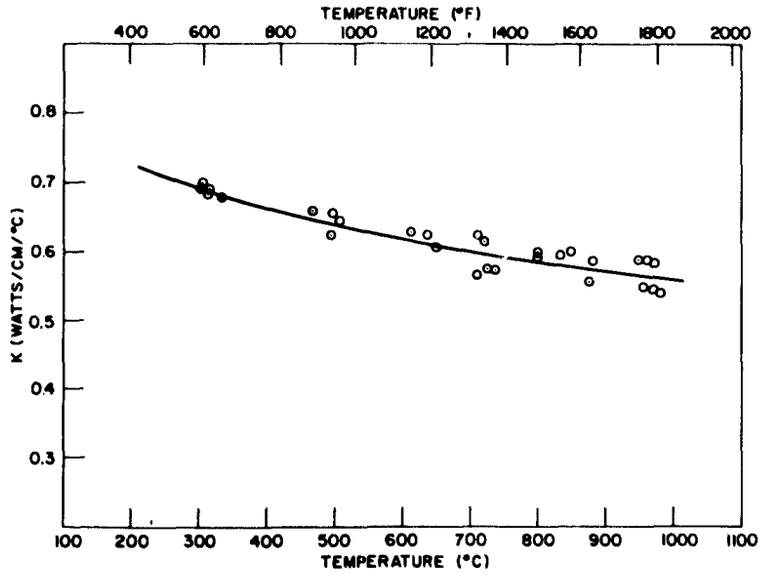

Fig. 12 — Thermal conductivity of sintered 75%-dense uninfiltrated tungsten.

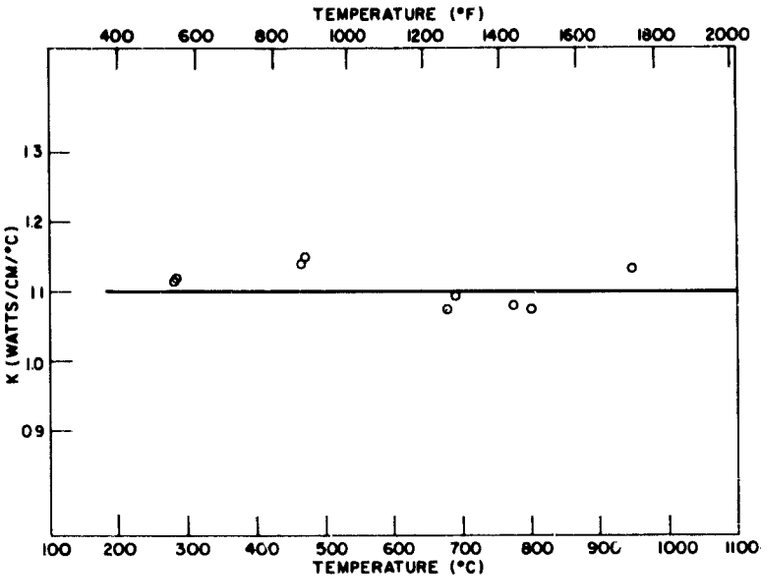

Fig. 13 – Thermal conductivity of sintered 80%-dense tungsten infiltrated with silver

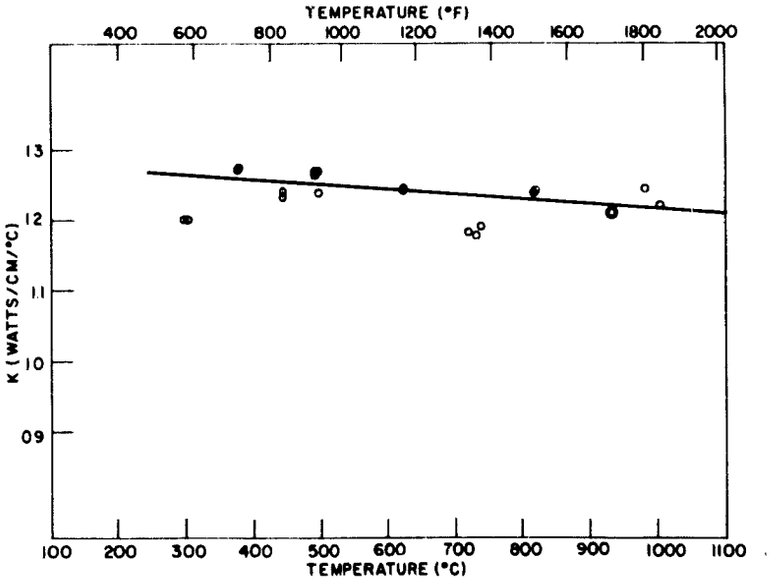

Fig. 14 – Thermal conductivity of sintered 80%-dense tungsten infiltrated with copper

TABLE 2
Analysis of Exhaust Gas Composition for Aerocel 163 Propellant*

Composition of Gases	Volume Percent of Gases
CO	29.3
CO_2	1.7
H_2	24.3
H_2O	12.2
HCl	7.2
N_2	11.40
H	8.73
OH	1.78
Cl	1.09
O_2	0.02
Al_2O_3(liquid)	41.45†

*Flame temperature = 6600°F; Oxidation ratio $\frac{O}{CO + Al_2O_3} = 1.107$.
†Weight percent of total.

for materials of good quality no fractures are induced. Hence, to extend the range of quality over which relative comparisons could be made, it was necessary to provide standard shaped stress-raisers in the model nozzle inserts. These have been discussed previously and were illustrated in the first few figures.

Figures 3 and 4 illustrate crack patterns for several specimens; however, the crack patterns can best be illustrated by sketching the cracks with the surface of the insert cylinder presented as a plane surface as shown in Fig. 15.

It was shown by the results of the strain measurements that the circumferential thermal stresses were greater than the axial thermal stresses by a factor of about four. The most severe notch was therefore the axial elox notch as shown on Fig 5. When several notches were on the same specimen, they were so placed with respect to each other so that they could be considered as independent. This independence might be lost if a large fracture developed in one notch.

Tables 3-5 summarize the effects of stress raisers on nozzle inserts, correlating a qualitative description of crack damage with material type. Under the heading Superficial Crack Description several arbitrary distinctions are made. The first two columns (In Root and Normal to Notch) tabulate the situations in which cracks appear when the specimen has been notched with stress raisers; the presence of a black mark in the appropriate position recording that a fracture was observed. Columns labeled Axial and Circumferential indicate the existence of cracks which could in no

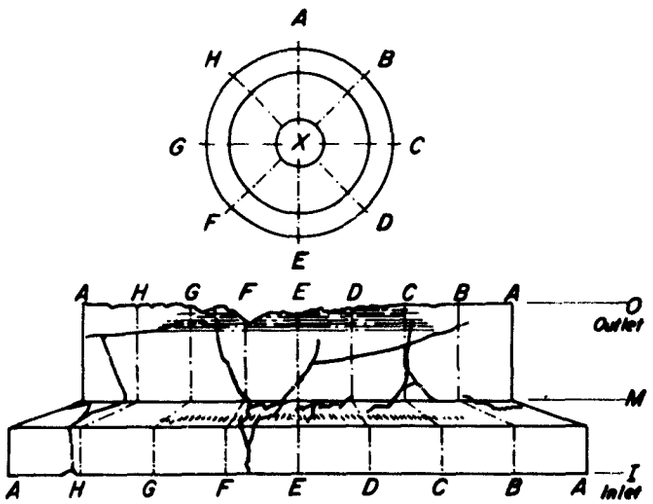

Fig. 15 — Crack pattern on outer surface of insert B-2

TABLE 3
Crack Damage Appearing in Uninfiltrated Sintered Tungsten Nozzles After Being Exposed to Flame Temperature of 6500°F for 30 Seconds

Firing Number	Notch Type	In Root	Superficial Crack Description*			Density Class (%)
			Normal To Notch	Axial	Circumferential	
3	none			■	■	80
7	4 nicks†	■			■	80
19	none			■	■	80
20	4 nicks†	■	■	■	■	80
23	Elox					90
26	Elox		■			90
27	Elox	■	■	■	■	80
‡	hoop					100
30	hoop	■	■	■	■	70

*Black rectangles indicate occurrence of visible thermal fracture lines
†Cracked in root of two deepest notches.
‡Allied Chemical sintered pellet.

TABLE 4
Crack Damage Appearing in Nozzles Made of Sintered Tungsten Infiltrated With Silver and After Exposure to Flame Temperature of 6500°F for 30 Seconds

Firing Number	Notch Type	In Root	Superficial Crack Description*			Density Class (%)
			Normal To Notch	Axial	Circumferential	
6	hoop	■				80
10	none			■	■	80
11	none					80
12	none					80
15	none					80
16	hoop	■				80
21	hoop	■	■			80

*Black rectangles indicate occurrence of visible thermal fracture lines.

TABLE 5
Crack Damage Appearing in Nozzles Made of Sintered Tungsten Infiltrated with Copper and After Exposure to Flame Temperature of 6500°F for 30 Seconds

Firing Number	Notch Type	In Root	Superficial Crack Description*			Density Class (%)
			Normal To Notch	Axial	Circumferential	
5	hoop					80
9	none					80
13	none					80
14	none					80
17	hoop	▬				80
18	hoop					80
22	none					90
24	Elox	▬				70
25	Elox	▬				90
28	hoop					70
29	Elox	▬				70

*Black rectangles indicate occurrence of visible thermal fracture lines.

obvious way be associated with the presence of a deliberately introduced stress raiser. The subheadings Axial and Circumferential are intended to suggest the predominate orientation of the cracks.

On this basis a relative quality rating for a material could be established by observing the number of black marks earned in each table. Thus, copper infiltrated tungsten in Table 5 with the least black marks ranks best, while uninfiltrated tungsten, Table 3, is the worst performer.

NOTCH BAR TEST RESULTS

The values of the toughness factor G_c obtained for the three types of material considered in this program are listed in Table 6. In general, the larger the value of G_c, the greater the amount of energy that is required to propagate the fracture and the more resistant the material will be to rupture. It is clear from these data that the introduction of silver or copper tends to produce larger values of G_c, and in particular these results support the conclusions of the nozzle insert stress-raiser tests, that copper infiltrated tungsten is a better performer than silver infiltrated tungsten or unfiltrated tungsten in the 70- to 90-percent-density ranges.

Although for a limited group of materials this agreement between static firing results and a laboratory fracture experiment is gratifying, it is not a broad enough basis for suggesting that the less expensive laboratory test is adequate to exclusively substitute for static firing experiments in evaluating the performance of these materials. Furthermore, there is no unqualified assurance that performance in model tests will be duplicated in full-scale structures. Much is to be learned from both procedures.

RESULTS OF STRAIN MEASUREMENTS

Typical results from the measurements of strain on the nozzle inserts during static firing are displayed in Figs. 16-19. As was discussed earlier, most of the gage installations were strongly responsive to temperature so that prefiring heating cycles had to be performed to obtain a curve for the resistance change of each unit as a function of

TABLE 6
Fracture Toughness Factors Derived from Notched Bar Tests at Room Temperature for the Three Basic Types of Materials Used in Nozzle Construction

Bar Identification	Tungsten Density (%)	Infiltrate Metal	G_c (in.-lb/in.^{2})	G_c Average
A-2	71	none	0.53	
A-5	71	none	0.70	0.62
1-C	79	none	0.50	
1-M	79	none	0.38	0.44
C-2	91	none	0.25	
C-3	91	none	0.20	
C-4	91	none	0.42	
C-5	91	none	0.37	0.31
IF	77	silver	3.41	
IG	77	silver	2.59	3.00
E-2	80	silver	1.54	
E-5	80	silver	1.43	1.49
109-7	80	silver	2.97	
109-8	80	silver	4.54	
109-9	80	silver	3.09	
109-10	80	silver	4.00	3.65
B-2	70	copper	6.60	
B-3	70	copper	6.96	
B-4	70	copper	6.55	
B-5	70	copper	7.16	6.82
TLO-7	76	copper	3.94	
TLI-4	76	copper	7.76	
TLI-6	76	copper	5.54	
TLI-7	76	copper	5.50	
TT-2	76	copper	6.12	
TT-5	76	copper	10.89	
TT-6	76	copper	5.59	
TT-7	76	copper	4.77	
TT-8	76	copper	6.54	6.29
IL	77	copper	5.17	
IN	77	copper	7.54	6.36
F-2	80	copper	4.68	
F-3	80	copper	5.31	5.00
D-3	86.5	copper	2.11	

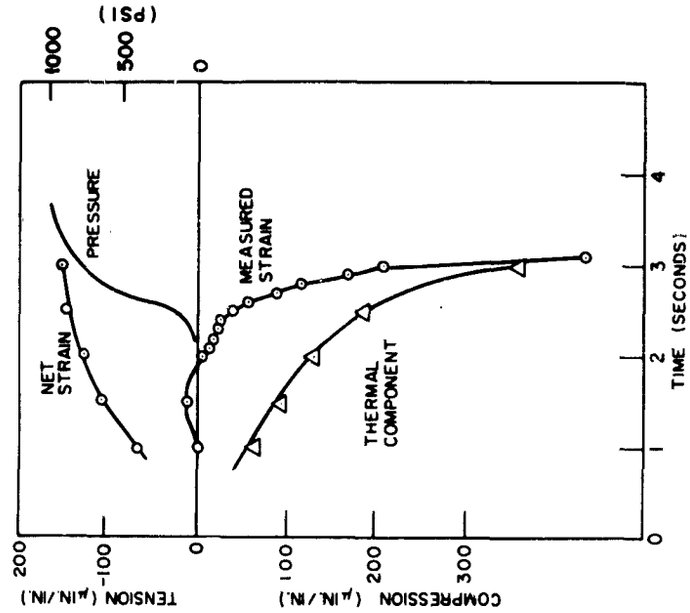

Fig. 17 — Axial strain measured with spot-welded foil gages on "cold" surface of copper infiltrated nozzle insert during initial stages of fuel ignition. The fuel chamber pressure curve is displayed in proper time sequence for relative comparison in arbitrary ordinate units.

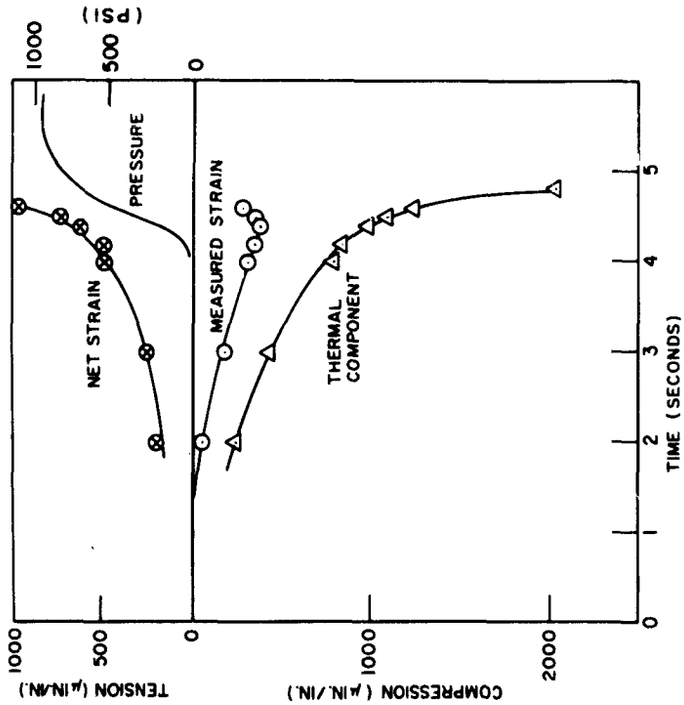

Fig. 16 — Circumferential strain measured with hoop gage on "cold" surface of a silver impregnated nozzle insert during initial stages of fuel ignition. The fuel chamber pressure curve is displayed in proper time sequence for relative comparison in arbitrary ordinate units.

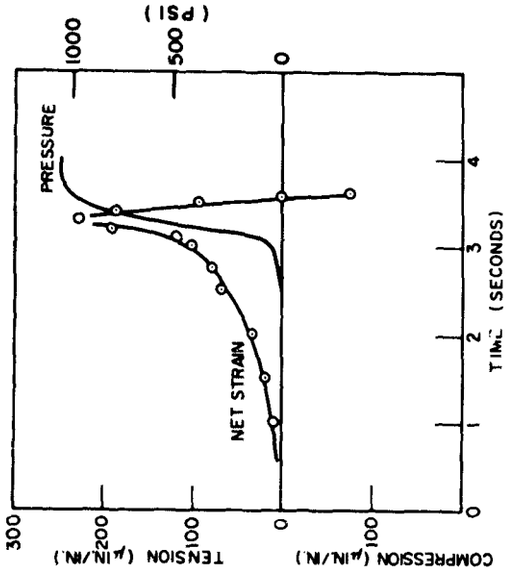

Fig. 19 – Axial strain measured with strippable foil gage on "cold" surface of silver impregnated nozzle insert during initial stages of fuel ignition. The fuel chamber pressure curve is displayed in proper time sequence for relative comparison in arbitrary ordinate units.

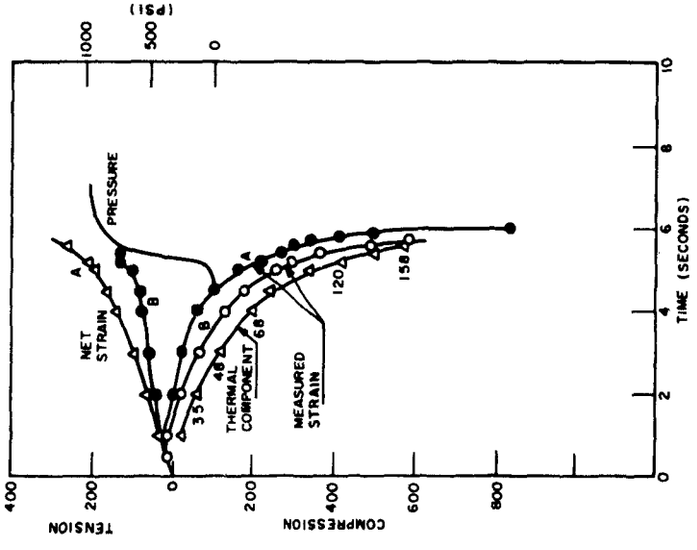

Fig. 18 – Axial strain measured simultaneously at two different circumferential locations with two spot-welded foil gages on "cold" surface of silver impregnated nozzle insert, during initial stages of fuel ignition. Numerals beside points on the Thermal Component curve indicate increase in surface temperature since ignition (°F).

temperature with the stress equal to zero. These changes in resistance data (see for example Fig. 7) are then converted into an equivalent strain for the measured temperature that existed on the nozzle insert surface.

This curve on each figure is labeled Thermal Component and consolidates the respective heating-cycle strain-corrections both in magnitude and algebraic sign. By subtraction from the curve labeled Measured Strain, the net strain caused by stress is obtained. In the case of Fig. 18, the two welded gages performed sufficiently alike in prefiring heat cycles that a single correction curve may be applied to either one.

A feature of the measured strain trace exhibited only by the welded type gages is the initial excursion on the tension or upper side of the strain coordinate. This is evident in both Figs. 17 and 18. It is suggested that this would be the case if a thermal lag existed for the welded mounting. The desired tension strain reading due to the thermal gradient in the nozzle insert wall is initially uncluttered by any signal related to an increase in temperature of the gage itself even though the temperature of the surface upon which it is mounted has begun to increase. This situation is only temporary and soon the thermal component becomes larger than the measured strain as heat is conducted through the welds and air gap to the strain gage sensing element.

The strippable foil transfer gage data shown in Fig. 19 exhibited negligible resistance change during a similar thermal test and required no correction for the measured strain readout. As mentioned previously the hoop type circumferential gage required the largest corrections as shown in Fig. 16. This need not be considered entirely a disadvantage however.

Strain resulting from the thermal gradient during the firing puts the material at the nozzle surface in tension and hence produces a change in gage resistance opposite to that associated with the simultaneous increase in temperature. Thus the combined signal tends to present a smaller amplitude to the recording system than would exist for each effect individually. Hence, larger amplification can be used for the recording channel or larger thermal shock strains accommodated by a given gain setting.

An interesting coincidence is illustrated by Figs. 20 and 21. Signals from two welded type strain gages are traced in Fig. 20 together with

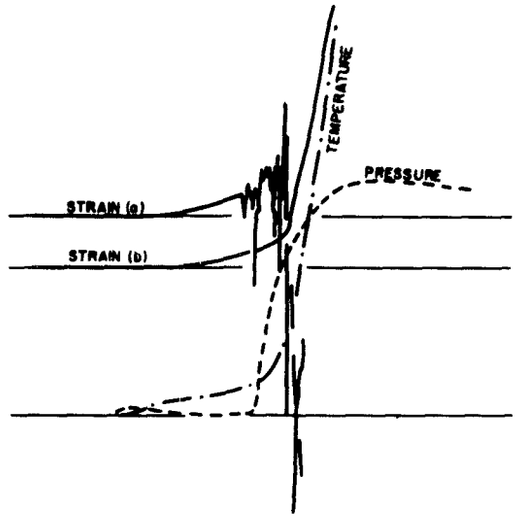

Fig. 20 — The curve (STRAIN (a)) is a tracing of a record showing a characteristic signal beginning a few seconds after ignition when a crack resulting from thermal distortion progressed under the area covered by a welded type strain gage. The curve (STRAIN (b)) is a similar reproduction for the simultaneously recorded signal from an adjacent welded type strain gage over an uncracked area. The insert was composed of 80%-dense uninfiltrated tungsten. A fuel chamber pressure curve and surface temperature signal from a thermocouple are also included in proper time sequence for relative comparison in arbitrary ordinate units.

the simultaneous recording of motor gas pressure and surface temperature of the nozzle insert. The relative positions of all these curves on the horizontal time axis is correct but the amplitides have been left uncalibrated. These gages were oriented so as to sense axial strain. Postfiring examination showed that a crack had run under strain gage No. 1 while the surface beneath gage No. 2 was intact. A clear-cut demonstration as to the time, and temperature, at which this crack occurs is of considerable importance. Figure 21 is an additional example in which a hoop or circumferential strain sensing type gage is underrun by a crack. Again the rupture begins early in the sequence before the motor pressure has reached equilibrium and before the surface temperature has exceeded much more than a few hundred degrees. The violent excursions of the signal trace no longer represent true distortion of the metal after the

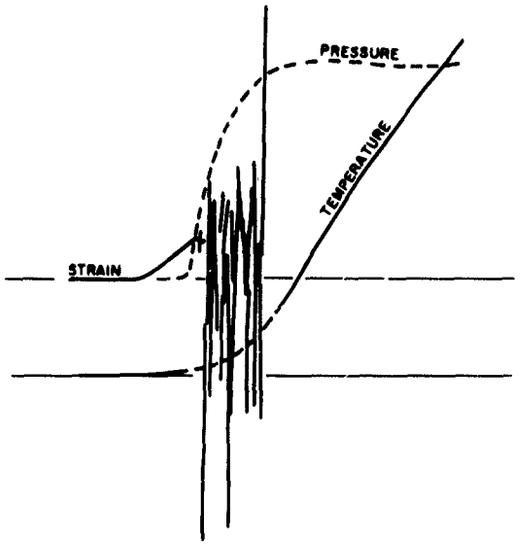

Fig. 21 – The curve (STRAIN) is a tracing of the recording for a signal from a hoop gage on an uninfiltrated 80%-dense tungsten insert. Shortly after the onset of fuel ignition thermal cracking under the gage produced the complex modulation on the record. A fuel chamber pressure curve and surface temperature thermocouple signal are also included in proper time sequence for relative comparison in arbitrary ordinate units.

crack appears since the conducting wire composing the gage is now being stretched across gaps.

Strain measurements were generally terminated a few hundred degrees above ambient. Previous workers (4, 5) have shown that the cold-surface stresses are near a maximum at this time, hence no great effort was made to extend the time of recording. Figure 18 provides an indication of the temperature scale and Fig. 19 provides one example where the maximum strain (caused by stress) has been attained. For the particular nozzle model configuration used in this program the result of the strain measurements can be summarized in the following statements:

1. The strain in the circumferential or hoop direction on the "cold" surface is larger by a factor of 3 or 4 times than that in the axial direction. It is not intended to imply that the material properties control this effect but rather the geometry of the nozzle insert. In long cylinders this ratio of circumferential to axial strain should be unity (4).

2. The maximum thermal stress (or equivalent strain) in both circumferential and axial directions attributed to thermal gradient appears very early in the ignition sequence, before full pressurization of the motor chamber occurs.*

3. When thermal cracking was observed in a given specimen, it took place early in ignition phase of the test as might be expected from the strain versus time pattern implied in statement 2. Further evidence was available, however, in examples of signals generated when cracking occurred within the area covered by a strain gage as well as metallographic study of the crack surface.

4. In the circumferential direction the observed strain reached a magnitude of about 1000 microinches per inch. Converting the strain readings to stress (using a Young's modulus of 50×10^6 psi for sintered ingot tungsten), the equivalent stress levels are about 50,000 psi. This value is approximately the tensile strength, and thermal fracture should be expected, especially in the presence of stress raisers. However, the stresses considered are biaxial with the principal strain axes being in an axial and a circumferential direction, so for the measured strains (maximum values) of 200×10^{-6} and 1000×10^{-6} in these respective directions, the calculated stresses are

$$\sigma_x = \frac{E(\epsilon_x + \epsilon_y)}{1 - \nu^2} = 28{,}000 \text{ psi}$$

$$\sigma_y = \frac{E(\epsilon_x + \epsilon_y)}{1 - \nu^2} = 106{,}000 \text{ psi}$$

where the subscript x refers to the axial direction and y refers to the circumferential direction. Poisson's ratio ν has been taken as 0.3. These results are in reasonable agreement with Vigness and Clements (4) and the work of Gordon and Brown (5), and will result in fracture if the material is in a brittle state. However, as very little plastic flow is necessary to relieve these stresses and the temperature is several hundred degrees above ambient temperature when the stress is maximum, the thermal stress problem should be solved by relatively small improvements of materials and techniques.

*Apparently the fuel used burned relatively slowly for a few seconds before pressure buildup; see section on Pressure Buildup Delay on page 20 of this report.

PRESSURE BUILDUP DELAY

There were relatively long and unequal delays between squib firing and pressure buildup during which a slow burning process heated the nozzle throat interior at a rate different from the full-scale condition. This uncertainty in the rate of initial nozzle temperature change would be expected to result in more scatter of experimental results in all phases of the test than would otherwise occur.

CONCLUSIONS

A method has been developed for rating in a relative manner the abilities of various rocket nozzle materials to withstand thermal stresses. This method consists principally in using a small rocket nozzle insert in a small rocket. The rocket fuel was selected to give temperatures, pressures, and firing times corresponding to that of a full-scale rocket. Various stress concentration factors could be introduced into the insert to extend the range of qualities of materials for which relative ratings could be obtained.

Results of tests on various nozzle insert materials showed that high density (near 100 percent) sintered high purity (hot-pressed spherical particles) tungsten and copper impregnated sintered tungsten rated relatively high. Silver impregnated rated somewhat lower, and, in general, sintered tungsten in the 70- to 85-percent-density range rated too poorly to be considered. Metallographic records and ratings of the nozzle inserts are included in Appendixes A, B, and C.

The fracture toughness factor G_c was also measured for the above materials and gave results consistent with the above conclusions.

Strain measurements were made using three different types of bonded electrical resistance gages and oriented in two directions, one parallel to the cylindrical axis and the other circumferential. For the particular nozzle insert geometry employed, the circumferential strain exceeded the axial strain by a factor of 3 or 4. This difference between axial and circumferential strain is attributed to the geometry of the model, the inner throat contour imposing a thicker wall section in the center of the insert with two thinner wall sections at the entrance and exit ends. The stresses computed from the maximum strain readings, particularly in the circumferential orientation, were as great as the tensile strength values assigned to the sintered ingot tungsten. Characteristic strain gage signals and postfiring metallographic examination of crack surfaces indicate that thermal cracking occurs very early in the ignition phase.

ACKNOWLEDGMENTS

This report is based principally on work directed by Eugene Olcott of the Atlantic Research Corporation under contract Nonr-3601(00)(X). The report also contains results of experiments performed by Dr. Hugh Romine at the U.S. Naval Weapons Laboratory, Dahlgren, Va., as well as data acquired by C. T. Ewing of the Chemistry Division of the U.S. Naval Research Laboratory. The initial metallographic studies were made by Dr. R.A. Meussner of the Metallurgy Division of the U.S. Naval Research Laboratory.

REFERENCES

1. Irwin, G.R., Kies, J.A., and Smith, H.L., Proc. Am. Soc. Test. Mat. 58:640 (1958)
2. Timoshenko, S., and Goodier, J.N., "Theory of Elasticity," 2nd ed., New York:McGraw-Hill, p. 60, 1951
3. Ewing, C.T., Walker, B.E., Jr., Miller, R.R. NRL Memo 6130-11, Feb. 15, 1963
4. Vigness, I., and Clements, E.W., "Numerical Method for Determining Thermal Stress Involving Plastic Flow," NRL Report 5765, May 24, 1962
5. Gordon, G.M., and Brown, D.A., "Tungsten and Rocket Motors," Stanford Research Institute, Progress Report No. 20, April 1, 1962

APPENDIX A
METALLURGICAL EXAMINATION OF FIRED TUNGSTEN ROCKET NOZZLE INSERTS

EUGENE L. OLCOTT
Atlantic Research Corporation
Alexandria, Virginia

The 29 tungsten inserts tested in the program described were metallographically examined after firing. Special attention was given to the extent of loss of infiltrant, any change in grain size, the extent of cracking, the penetration of aluminum oxide into the pores, and any other significant microstructural characteristics which could be observed. The first two inserts, B-1 and B-2, were examined by the Physical Metallurgy Branch of the Naval Research Laboratory and are described in detail in Appendix B. The third and fourth inserts, B-3 and B-4, were examined but not reported on by the Naval Research Laboratory and so are included in this discussion.

Most of the pressed and sintered tungsten was made by General Electric Company to 80% nominal density and infiltrated by Mallory Metallurgical Division. This material was used in firings B-1 through B-15 inclusive and also in firings B-19, B-20, and B-27. The balance of the material was pressed and sintered by Mallory and also infiltrated by Mallory. This material bears the Mallory designations which are 5S for 80%-dense tungsten, silver infiltrated; 35W3 for 70%-dense tungsten, copper infiltrated; 50W3 for 80%-dense tungsten, copper infiltrated; and 60W3 for 88%-dense tungsten, copper infiltrated.

It will be noted that the Mallory 5S material is nominally equivalent to the silver infiltrated General Electric material. A comparison of the grain size of these similar materials was made in the area of the expansion section of the fired nozzles. This area receives the least total heat input of any part of the inserts, but even so it is likely that some slight grain growth may occur from the firing cycle. The General Electric materials showed a grain size range of 6 to 20 microns. A typical pore size was 10×16 microns. The Mallory material showed a grain size of 2 to 12 microns. The pores were more rounded and were approximately 8 microns in diameter. The 70%-dense Mallory material, such as used in firing B-18, showed an even finer grain size, 1 to 6 microns.

No significant changes in grain size were observed at the throat section of any of the inserts. Abnormal grain growth does not ordinarily occur with pressed and sintered tungsten material. Minor grain growth was observed on all of the inserts at the throat section where, for a depth of several grains, the smallest grain size was approximately that of the largest grains of the unaffected material.

Previous experience had indicated that the fine cracks resulting from thermal stresses during firing could, in many cases, be determined only on a polished cross section. Even penetrant dye did not reliably indicate the presence of cracks of infiltrated materials. Also, in the case where notches were present, the root of the notch would show indications whether or not a crack was present. Therefore, the polished cross section of the nozzle was used as a plane of comparison among the different inserts for establishing the extent of cracking. It is possible that a different degree of cracking occurred on a different cross section, and therefore the particular cross section selected for examination may not have been representative in some cases. In general, however, the cracks observed were long cracks, usually extending around the entire periphery, and it is not believed that any substantial variation in extent of cracking occurs throughout the mass of the insert. The varying notch geometry influenced the cracking to some extent. It was observed that with circumferential V-notches the more crack resistant composites did not crack even when this notch was present. However, the deep Elox axial grooves caused cracking in every case. Therefore, the particular inserts which had this type groove had at least one additional crack present because of the groove.

The results of the metallographic examinations are shown in Table A1. Extent of cracking is designated by a number from 1-5 with the severity increasing with higher numbers. The maximum depletion zone for infiltrated materials is measured from the gas side to a depth where approximately one-half of the infiltrant has disappeared. In the case of the uninfiltrated material, the dimension shown in the depletion column is the depth of penetration of aluminum oxide into the porous material. The polished cross sections of most of the nozzles showed a substantial variation in pore extent.

Macroexamination of the polished cross section showed a number of zones of varying reflectivity. In the case of the uninfiltrated material, the portion of the insert penetrated by aluminum oxide was more reflective. Also, this more reflective area showed larger pores as if the higher temperature in this zone and the aluminum oxide penetration tended to increase the pore size. In the case of the infiltrated material, the greater reflectivity zones were largely depletion zones.

Substantial variations in microstructure occurred in any given insert. Several of the inserts showed local areas which were almost pore free. Other areas would contain pores of varying size. It cannot be established at this time whether this variation in microstructure was caused by the firing cycle or by an initial variation present from the facrication process. It is possible that either silver or copper would facilitate sintering during the firing operation and permit relatively pore-free areas to occur.

No significant reactions of the tungsten could be observed at the hot gas interface. A few areas showed pore enlargement and indications of possible oxide formation, probably a tungsten aluminate. This reaction can be considered to be of a minor extent and does not cause any appreciable losses of the tungsten with the propellant used in the firings. In a number of cases a thin carbide layer formed on the outside of the insert by reaction with the carbon backup material. In one case (firing B-15), a short crack was associated with the presence of the carbide layer.

The variations in the extent of depletion is difficult to understand. Several of the inserts, such as that of firing B-22, showed essentially no loss of copper. Similarly, the insert of firing B-11 showed very little silver depletion. It is noteworthy that the inserts which showed the least depletion also showed little or no cracking.

In order to visually compare the extent of cracking among the various inserts, a bar graph (Fig. A1) was prepared. Each bar represents a group of firings of the same basic material. The numbers 1 to 5 represent the extent of cracking as explained in Table A1. The firing numbers are listed and located with respect to their crack rating. The height of the bar corresponds to the highest crack rating of the particular material. It can be observed that the Mallory 70% copper infiltrated material, the General Electric 80% copper infiltrated material, the Mallory 88% copper infiltrated material, and the Mallory 70% dense material showed the least cracking. The 80%-dense General Electric material with silver infiltrant was next in order of least cracking, followed by the similar material pressed, sintered, and infiltrated by Mallory (5S). The uninfiltrated materials cracked and showed scatter in their results. In general, it can be noted that these thermal stress fracture results correlate with the fracture toughness results described in the previous portion of the report. In Fig. A2 the test specimens are arranged according to the same rating scale used in Fig. A1 but without regard for density or manufacturer. This permits the metallographic results to be compared directly with the charts of superficial damage (Tables 3-5) presented earlier. Again the copper infiltrated material ranks best by having the least score on the damage scale.

TABLE A1
Results of Metallographic Examinations

Firing No	Material	Type of Notch	Cracking on Cross Section	Crack Rating Number*	Visual Appearance of Polished Cross Section	Microscopic Observations
B-3	80%-dense W (GE)	Circumferential V	2 cracks 3/4 of thickness	4	3/8" deep reflective zone at entrance (Al_2O_3 penetration)	Divergent section less porous
B-4	80%-dense W (GE), Ag infiltrated (Mallory)	Circumferential V	Fractured at notch after 30 sec (longer duration than others). Numerous laminar cracks at entrance.	5	Not polished. After insert fractured and ejected exit end, leakage occurred around remaining portion.	
B-5	80%-dense W (GE), Cu infiltrated (Mallory)	Circumferential V	None	1	3/8" deep depletion zone at entrance. Somewhat mottled appearance.	Some depletion and pore enlargement on outside
B-6	80%-dense W (GE), Ag infiltrated (Mallory)	Circumferential V	2 fine 1/8" cracks at notch root	3	3/16" depletion zone at entrance	Material behind depletion zone appears to be about 90%-dense tungsten. Depletion zone appearance corresponds to 80% nominal density
B-7	80%-dense W (GE)	4 circumferential notches of varying depth	2 deep cracks and 2 short cold side and 1 hot side	5	Mottled, non uniform	Expansion section and other areas near OD are relatively pore free
B-9	80%-dense W (GE), Cu infiltrated (Mallory)	None	Laminar hot side approach cracks	2	3/16" depletion zone at entrance. Mottled, non uniform	Some general depletion Some dense areas
B-10	80%-dense W (GE), Ag infiltrated (Mallory)	None	2 cracks 2/3 of thickness 1 crack laminar hot side	5	Mottled, non uniform	Thin dense area on gas side. Depletion zone about 3/16". Pore structure on expansion section looks like 70%-dense tungsten. Some other areas show few pores.
B-11	80%-dense W (GE), Ag infiltrated (Mallory)	None	Laminar cracks on hot side	2	Uniform	Very thin depletion area. No general depletion. Some areas of low void content.
B-12	80%-dense W (GE), Ag infiltrated (Mallory)	None	Laminar cracks on hot side	2	Uniform. 5/16" depletion layer	Area behind depletion layer and other scattered areas show void content
B-13	80%-dense W (GE), Cu infiltrated (Mallory)	None	None	1	5/16" depletion zone at entrance. Mottled appearance	Depletion zone showed very low copper loss
B-14	80%-dense W (GE), Cu infiltrated (Mallory)	None	None	1	5/16" depletion zone at entrance. Mottled appearance	Actual depletion zone is 1/8" deep. Most of balance of cross section shows low void content. Some areas very dense
B-15	80%-dense W (GE), Ag infiltrated (Mallory)	None	2 laminar cracks on OD	2	1/4" depletion zone at entrance. Uniform	Some carbide formation on OD at cracked area

*Crack Rating Number
1 = no cracks in polished section.
2 = only short laminar cracks.
3 = 2 cracks less than half the total thickness.
4 = 2 cracks more than half the total thickness.
5 = heavy cracks.

TABLE A1 (Continued)
Results of Metallographic Examinations

Firing No.	Material	Type of Notch	Cracking on Cross Section	Crack Rating Number*	Visual Appearance of Polished Cross Section	Microscopic Observations
B-16	80%-dense W, Ag infiltrated (Mallory 5S)	Circumferential V	2 cracks at notch root 3/4 through thickness	4	Uniform	Very little depletion
B-17	80%-dense W, Cu infiltrated (Mallory 50W3)	Circumferential V	2 cracks half way through	3	Uniform	Almost no depletion. Some areas of low void content.
B-18	70%-dense W, Cu infiltrated (Mallory 35W3)	Circumferential V	1 laminar hot side crack	2	3/8" depletion zone at entrance. Uniform.	Increased porosity on gas side. Some low void content in expansion area. Heavy depletion.
B-19	80%-dense W (GE)	None	2 cracks 3/5 of thickness	4	Mottled	Low void content on expansion end
B-20	Same	4 circumferential notches of varying depth	2 cracks 4/5 of thickness	5	Mottled	Considerable depletion
B-21	80%-dense W, Ag infiltrated (Mallory 5S)	Circumferential V	2 cracks 2/3 of thickness one of which was at notch root	4	Mottled	Considerable depletion
B-22	88%-dense W, Cu infiltrated (Mallory 60W3)	None	None	1	Uniform	No copper loss. Uniform. Appears to be of higher density and greater copper content than 60W3.
B-23	88%-dense W (Mallory)	None	2 cracks 2/3 of thickness	4	Uniform	Uniform, low void content
B-24	70%-dense W, Cu (Mallory)	Axial	Short crack in notch. 1 laminar crack on hot side.	2	3/8" depletion zone at entrance. Uniform. (Al_2O_3 penetration)	Uniform
B-25	88%-dense W, Cu infiltrated (Mallory 60W3)	Axial	Crack in notch 1 short cold side crack	2	Uniform	No depletion. Uniform
B-26	88%-dense W (Mallory)	Axial	Short crack in notch. 2 cracks 2/3 of thickness	4	Uniform	Low void content.
B-27	80%-dense W (GE)	Axial	Short crack in notch. 2 cracks 2/3 of thickness	4	5/16" Al_2O_3 filled zone at entrance. Mottled.	A few areas of low void content. Some high void content areas near OD.
B-28	70%-dense W, Cu infiltrated	Circumferential V	None	1	3/8" depletion zone at entrance. Mottled	Considerable depletion. Uniform
B-29	70%-dense W, Cu infiltrated (Mallory 35W3)	Axial	1 crack in notch	2	5/16" depletion zone at entrance Mottled.	Fairly uniform.
B-30	70%-dense W (Mallory)	Circumferential V	Fractured at notch. 1 crack at fillet. 4/5 of thickness	4	Uniform (entrance portion only available)	Fairly uniform (entrance portion only available)

*Crack Rating Number
1 = no cracks in polished section.
2 = only short laminar cracks.
3 = 2 cracks less than half the total thickness.
4 = 2 cracks more than half the total thickness.
5 = heavy cracks.

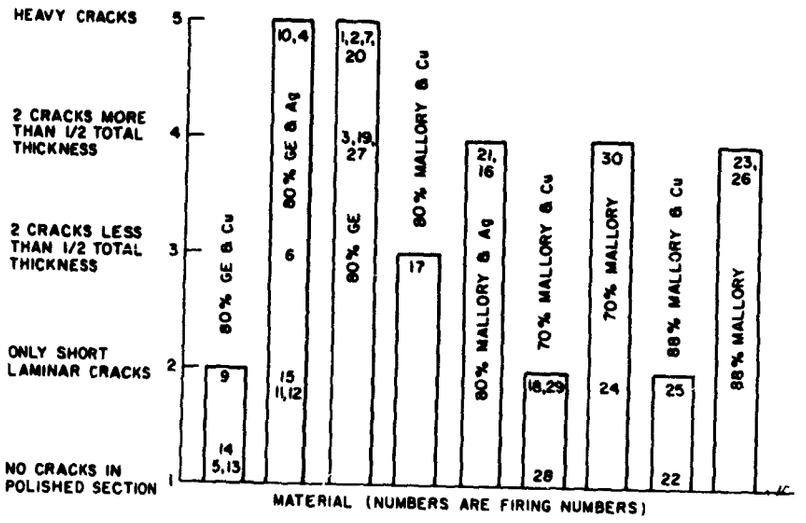

Fig. A1 — Extent of cracking of tungsten inserts grouped by densities

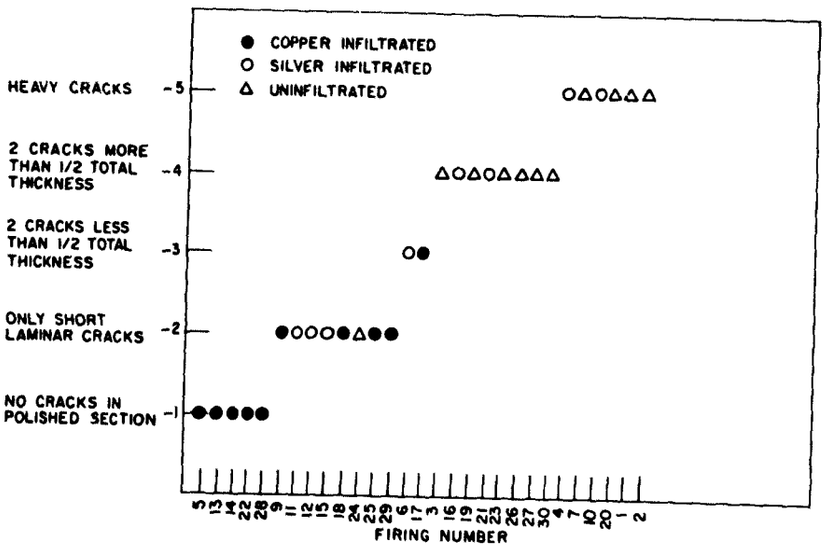

Fig. A2 — Extent of cracking of tungsten inserts grouped by crack rating number

APPENDIX B
METALLURGICAL EXAMINATIONS OF TWO EXPERIMENTAL TUNGSTEN ROCKET NOZZLE INSERTS (B-1 AND B-2)

R. A. MEUSSNER AND R. J. GOODE
Physical Metallurgy Branch
Metallurgy Division

Two sub-scale, tungsten, nozzle inserts from a continuing experimental study of thermal cracking have been examined in detail. These two heavy walled inserts were quite similar in design and manufacture and had been subjected to the same type of firing tests. Although both displayed equally satisfactory performance in these tests, one developed a large number of circumferential cracks while the other formed only one. The structure of the heavily cracked insert showed a non-uniform distribution of porosity and a limited zone of alumina infiltration. The other, was very uniform in structure and was completely infiltrated by alumina during its test.

The detailed examinations of these inserts revealed that, with the exception of the extent of the circumferential cracking, both had suffered the same type of damage. Both showed pitting and cracking along the entrance surface and both had developed deep longitudinal cracks in the body of the inserts. The cracking at the pit sites has been ascribed to contamination that resulted in hot tearing during the cooling of the parts after the tests. The longitudinal cracks, formed by thermal shock, were formed very early in the firing tests. In these small heavy-walled inserts these inherently dangerous cracks did not cause the nozzle to fail. From the mode of fracture and the extent of carburization along the circumferential cracks, it was concluded that these must form after the inserts had reached a high temperature. From these present observations, however, it has been impossible to decide whether these cracks formed several seconds after the initiation of the firing test, in which case they must be considered potentially damaging, or whether they formed early in the cooling stage after the test, when they could no longer affect the test results. Lacking a meaningful estimate of the time of formation of cracks of this type in these inserts, it is not possible to assess the comparative effects of the structures of these two inserts on the generation of damaging defects.

INTRODUCTION

Heavy-walled tungsten inserts remain the most promising of the few candidate materials for the construction of rocket nozzles. However, thermal cracking of these parts also remains a serious problem in adapting this material to this very critical application. The Mechanics Division, as part of their program on thermal cracking, has initiated an experimental study of the problem. Two sub-size nozzle inserts from this program were submitted to the Metallurgy Division for examination. These inserts, machined from the same pressed and sintered powder metallurgy blanks (Ca. 80% dense), had been subjected to identical test firings at the Atlantic Research Corporation's facility. The fuel was of the aluminized type and had a flame temperature somewhat in excess of the melting point of pure tungsten (3380°C, 6120°F). In assembling the test motor, the outer surfaces of the tungsten insert were coated with a slurry of MgO in phosphoric acid before the insert was placed in the carbon backup block. A heat shield, normally located aft of the insert, was omitted in the tests of both inserts and, as a consequence, a portion of the steel motor closure was melted in each test. This steel contaminated the exit end of both inserts and caused erosion and spalling at the end. Thermocouples at the carbon block: insert interface indicated that the thermal flux through these two inserts was very similar during the first part of the test (that is, up to the time that the thermocouples were destroyed by excessive temperatures).

NRL Problem No. R05-24C; Bureau Problem No. RR 011-05-X. This is an interim report. Work on this problem is continuing.

INSERTS

Prior to being submitted for this study, both inserts had been cleaned of most of the surface

oxides to permit measurements of the throat diameters and an examination of the surfaces to detect cracks formed during the test. Insert B-1 had been sectioned transverse to the throat axis just below the entrance collar section and the exit portion of this insert had been broken into two parts. Insert B-2 had been sectioned along the throat axis and, since the two halves appeared to be very similar, only one half of this insert was examined.

MACROEXAMINATIONS

Photographs of the pieces of insert B-1 are shown in Fig. B1 and a schematic representation of the crack pattern observed on the external surfaces of this insert is shown in Fig. B2. The lettered locator code indicated in these figures is provided to orient the parts in the photographs with the crack-map and will be used to indicate the locations of the sections cited in the discussion of the microexaminations. Figure B1a shows the sectioned surface of the entrance portion and the exit end of the reassembled pieces of the exit portion (a metallographic specimen had been removed at A-B before the photographs of Fig. B1 were taken). The effects of the contamination of the exit end of the insert can be clearly seen in Fig. B1a and a few of the most prominent cracks can be discerned on the cylindrical surface of this part. The strong line at F is not a crack formed during the test; it is the fracture formed after the test in breaking this section into two parts. Three or four of the many cracks in the fillet section of the insert are visible in the polished section. These penetrate to the edge of the alumina-infiltrated zone surrounding the throat. (The demarcation between the alumina-infiltrated region and the remainder of the insert is not shown to advantage in this photograph - see Fig. B3.) The heavy tool marks, extending from C to G along the fillet and in the cylindrical surface near the exit end of the insert, are indicated in Fig. B2 and are visible in this photograph. From the sketch of Fig. B2 and the photograph of Fig. B1a, it is evident that the fillet section is most severely cracked. Both circumferential and longitudinal cracks formed in the exit section and two longitudinal cracks traversed the collar section. From this crack pattern it appears that the tool marks alter neither the population nor the path of the cracks.

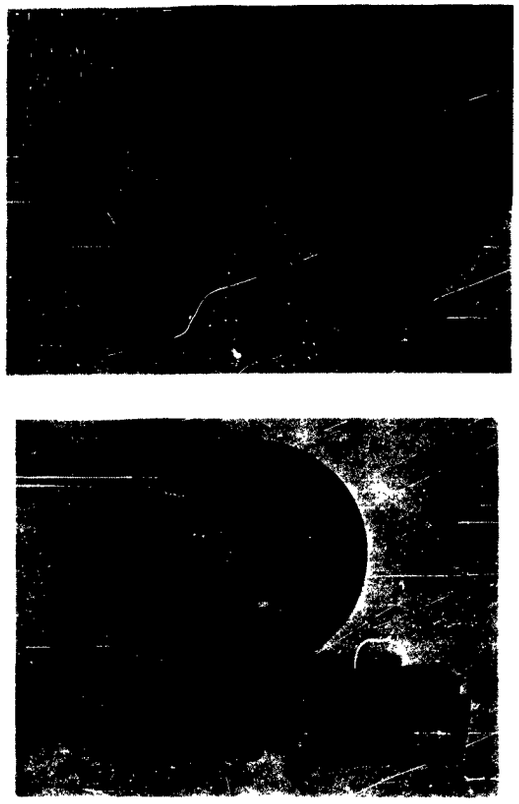

Fig. B1 — Photographs of insert B-1 (approximately full size)

Figure B1b shows the pitted entrance surface and the longitudinal fracture surfaces formed in breaking the exit portion of this insert in two. In these longitudinal sections, the depth of the contamination damage at the exit is revealed and one of the circumferential cracks is visible in the polished section at A and the fracture surface at B. The throat, while generally quite smooth, shows a few small elongated sites of attack near the entrance and a thin adherent oxide layer covering most of the remainder of its length.

The external surfaces of insert B-2 were quite similar to those of B-1. The entrance surface was pitted, the throat smooth but coated with a thin oxide layer, and the exit surface had been damaged by contamination with molten steel. This insert differed in design from B-1 only in that the fillet radius at the juncture of the entrance

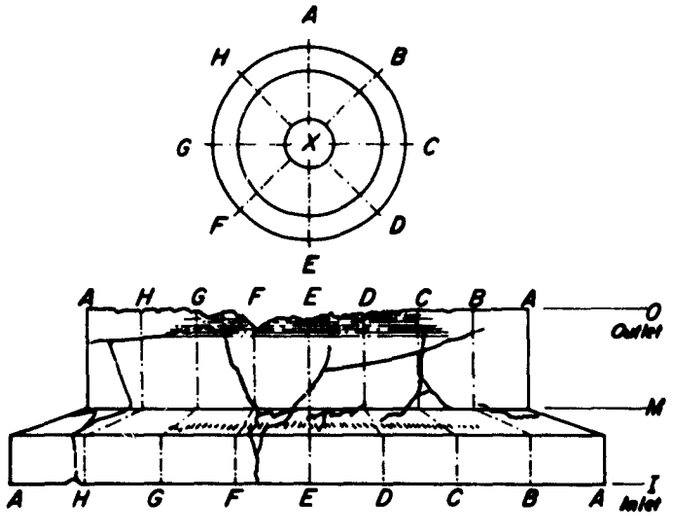

Fig. B2 – Crack pattern on outer surface of nozzle insert

collar and the exit section had been made much smaller (compare Figs. B3 and B4). In spite of this apparently less favorable design, the external surfaces of B-2 were almost free of cracks after the test firing. An examination of the surfaces of the insert revealed only one circumferential crack and this crack did not originate in the sharp fillet section. A longitudinal section of the insert containing a part of this crack is shown in Fig. B4.

The dark-field photomacrographs of longitudinal sections of these two inserts, Figs. B3 and B4, illustrate the general pattern of the damage in the inserts. Both show internal cracking beneath the pitted entrance surface and extensive damage in the contaminated exit area. The depth to which alumina from the flame has penetrated insert B-1 is defined by the smooth contoured light zone along the throat in Fig. B3. No similar boundary is delineated in B-2, Fig. B4, because the alumina has almost completely permeated the body of the insert. Except for a small triangular region along the outer surface above the contaminated area at the exit and an unusual small pocket midway along the throat surface, almost all of the pores were filled with aluminum oxide. Circumferential cracks, and the existence of enlarged pores along these, are clearly shown in both figures.

SPECTROCHEMICAL AND X-RAY DIFFRACTION DATA

Based on the microexaminations of the structures of these inserts, specimens from selected areas of insert B-1 were subjected to qualitative analyses by spectrochemical and x-ray diffraction techniques. Comparisons of the microstructures and the etching characteristics of the individual phases in the two inserts have shown that the observations collected in Tables B1 and B2 are applicable to both B-1 and B-2.

These data confirm the observation that the deterioration of the exit ends of these inserts was caused by steel contamination during the tests. The increased concentration of Fe, Ni, Cr, Si, and Mo found in this region can be attributed to this event. The aluminum, present as α Al_2O_3, is derived from the fuel. The source of the magnesium is probably the MgO slurry coating applied to the outer surfaces of the insert during the assembly of the motor. The x-ray data from this region indicate that the contamination has produced the "Fe_7W_6" or zeta phase* of the W-Fe system.

*Phase designation employed by M. Hansen in "Constitution of Binary Alloys" – McGraw-Hill (1958).

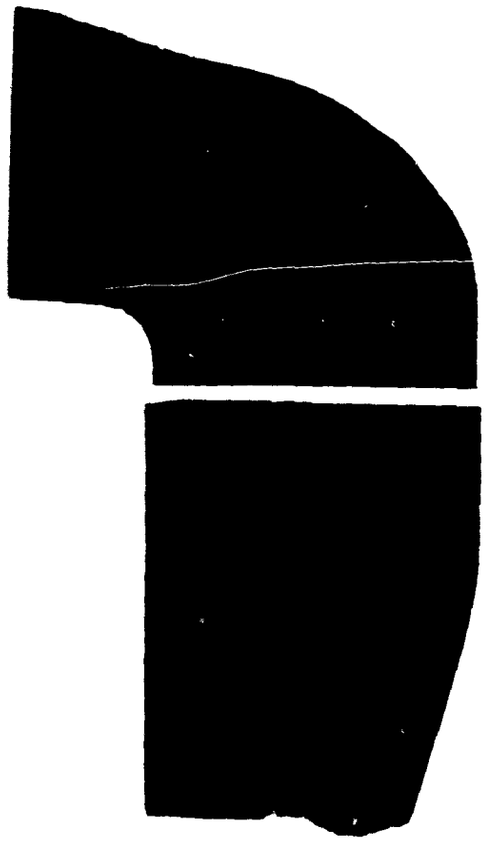

Fig. B3 – Longitudinal section of B-1 at A-B position (NaOH etch). (a)Entrance section 6.6X, (b)Exit section 7X.

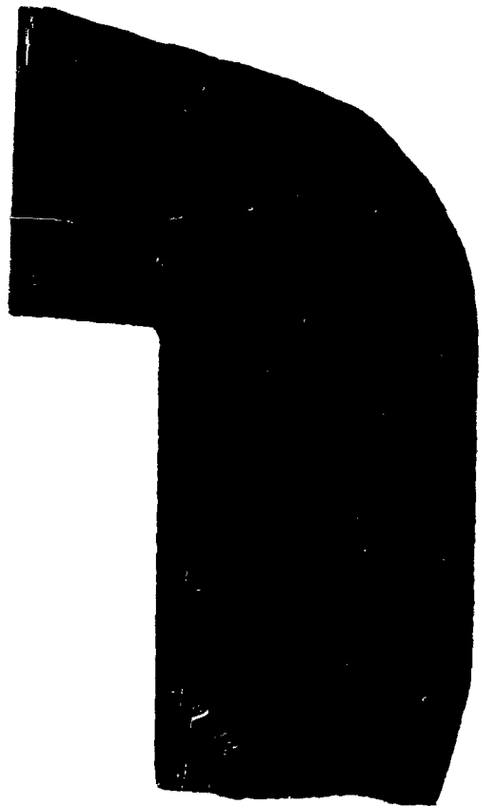

Fig. B4 – Longitudinal section of B-2 (NaOH etch) 4.7X

TABLE B1
Spectrochemical Analyses of Specimens from B-1

Specimen	Intensity*									
	W	Al	Fe	Ni	Cr	Mg	Si	Mn	V	Mo
Uncontaminated material	VS	VW	W	VW	VW	VW	W	VW	VW	Tr
Contaminated exit	VS	M-S	VS	W-M	S	W	W-M	W	Tr	W
Oxide-Contaminated exit	VS	VS	S	VW	S	S	M	M	VW	M
Entrance surface unpitted	VS	VS	M	W	W	M	M	W	W	W-M
Entrance surface pitted	VS	VS	S	M	M	M	S	W		VW
Oxide-Throat	VS	VS	M	VW	VW-W	M-S	S-VS	VW	VW	W

*VS 10-100%, S 1-10%, M 0.1-1%, W 0.01-0.1%, VW 0.001-0.01%.

TABLE B2
X-ray Diffraction Results from Specimens of B-1*

Specimen	Predominate Phases	Minor Phases	Remarks
Metal – Contaminated exit	W	Fe_7W_6	
Oxide – Contaminated exit	α Al_2O_3	$FeO{\cdot}Al_2O_3$ and/or Mg(Al, Fe)O4	
Metal-pitted entrance surface	W	α Al_2O_3	Some unidentified phase
Oxide-Throat	α Al_2O_3	$Mg(Al, Fe)O_4$ possible	Some unidentified lines – perhaps a silicate
Outer surface collar†	WC, W_2C		

*Filtered Cu radiation.
†X-ray defractometer trace from B-1 and B-2, all others powder patterns (114.7 mm camera).

Fig. B5 – Contaminated area at exit end of B-1, 500X. (a) NaOH etch, (b) NaOH and (b) NaOH and Cp-4 etch.

The pitted entrance surface and the internal cracking beneath these affected areas may also be attributed to contamination during the tests. The spectrochemical data show an increase in the concentration of Fe, Ni, Cr, Mg, and Si in these areas. Except for the high concentration of silicon, these chemical data could be attributed to steel and MgO contamination. The source of the steel contamination on this surface is not obvious, but it may come from the oxidation of interior parts of the motor case. The x-ray diffraction patterns of material from this area indicated W and α Al_2O_3 and contained only a few unidentifiable weak lines.

METALLOGRAPHIC EXAMINATIONS

Evidence of Contamination

The metallographic examinations of the structures of the contaminated regions along the entrance surface and at the exit of both inserts, B-1 and B-2, indicated that the same type of contamination and reactions had occurred in both tests. The affected regions were detectably more dense than the surrounding material and contained a distinct second phase – in addition to porosity and pores filled with aluminum oxide. However, the second phase, produced by the contaminant, was distinctly different in these two areas. At the exit end of the inserts, where the contamination was unquestionably the steel of the motor closure, the zeta phase of the W-Fe system was detected by x-ray diffraction. This phase was attacked by both the sodium hydroxide* and CP-4† etchants. Figures B5a and B5b show the same area etched with sodium hydroxide and consecutively etched with sodium hydroxide and CP-4. The sodium

*5 wt-% NaOH in water.
†5 ml HF, 5 ml HNO_3, 8 ml HAc.

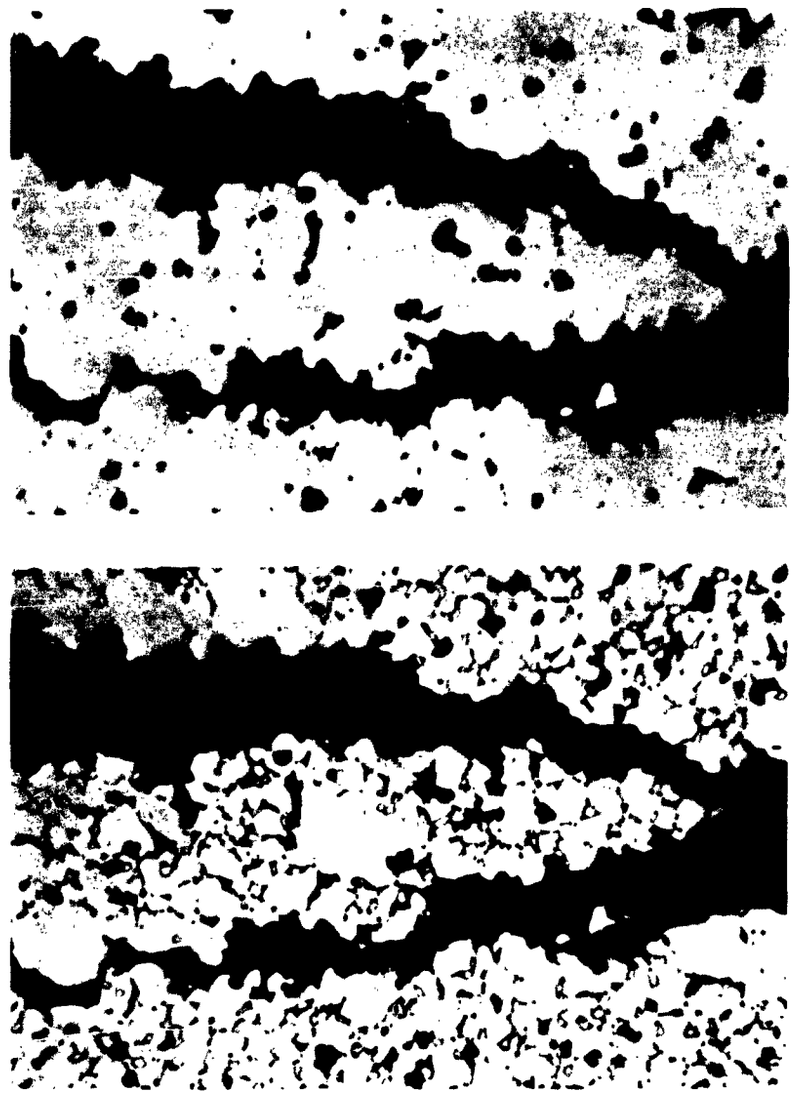

Fig. B6 — Contaminated area at entrance end of B-1, 500X. (a) NaOH etch, (b) NaOH and CP-4 etch.

hydroxide tends to stain the zeta phase. The CP-4 removes this stain, outlines the zeta phase more strongly, but reveals no additional phases in the structure. When this same etching procedure was applied to the contaminated areas along the entrance surfaces a very different behavior was observed. Figures B6a and B6b show the structure in this region after being etched with sodium hydroxide and sodium hydroxide followed by CP-4. The second phase, clearly defined by the CP-4 reagent, is unaffected by the hydroxide. The similarity of the etching characteristics and appearance of this phase and the W_2C phase found along the outer surface of the insert (see Fig. B7) suggests that the contaminant responsible for the deterioration along the entrance surface is carbon and that the second phase is W_2C. Since the areas containing a substantial population of these

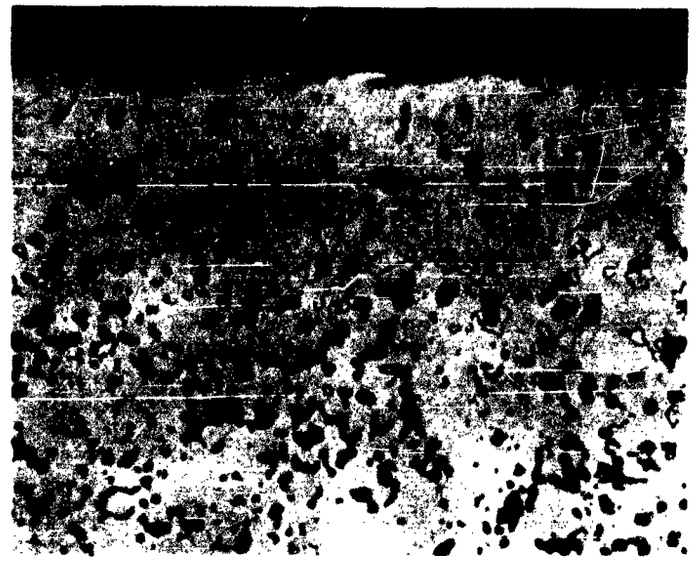

Fig. B7 – Tungsten carbide (W_2C) layer along the outer surface of B-2 (Cp-4 etch) 500X

second phase particles, as in Fig. B6, were very small, the sample used for the x-ray study probably contained too low a concentration of this phase to permit its identification.

The x-ray diffraction patterns from the outer surface of the collar sections of B-1 and B-2 indicated that these surfaces were heavily coated with WC and W_2C. Metallographic examinations showed that this coating of carbides extended over most of the outer surfaces of these two inserts but that the thickness of the coat and its continuity was much greater on B-2 than on B-1. The carbon back-up block is the most obvious source of this contamination and from the observed distribution of the carbide phase in the inserts it is reasonable to assume that the transfer of carbon was accomplished through a gaseous species. A photomicrograph of a section including the outer surface of B-2 is shown in Fig. B7. The coating is almost entirely W_2C at this site and penetration of the carbide phase along the pores of the structure has been limited to a rather thin zone in this specimen. The prevention of deep carburization in the B-2 insert may be attributed either to the rapid filling of the pores with aluminum oxide or to the formation of a continuous carbide layer on the surface. A continuous carbide layer, separating the interior porosity of the insert from the carbon source, would limit the carbon activity to that of W_2C or, at most, to that of WC. This sealing of the surface appears to be the decisive mechanism since the interior of the uninfiltrated insert, B-1, did not show excessive carbide formation except in the vicinity of some of the cracks.

Most of the pores were filled with aluminum oxide within the regions infiltrated by molten aluminum oxide from the flame. These pores, shown in the right section of Fig. B8a were much larger and of different form than those in the adjacent uninfiltrated portions of insert B-1. In fact, the uninfiltrated region of Fig. B8a and that of Fig. B8b appeared to be remarkably free of porosity when examined in the unetched condition. The fine interparticle porosity shown in these two photomicrographs was made evident by etching with the CP-4 solution. This delineation of the porosity by the etchant may be the result of the removal of flowed metal from the specimen surface by the etchant. Thus, the structures of these two figures may show a slightly exaggerated representation of the incomplete bonding among the tungsten particles. However, the distribution of this type of porosity in the uninfiltrated portion of the insert was not uniform, and Fig. B8b is representative of the areas showing very high

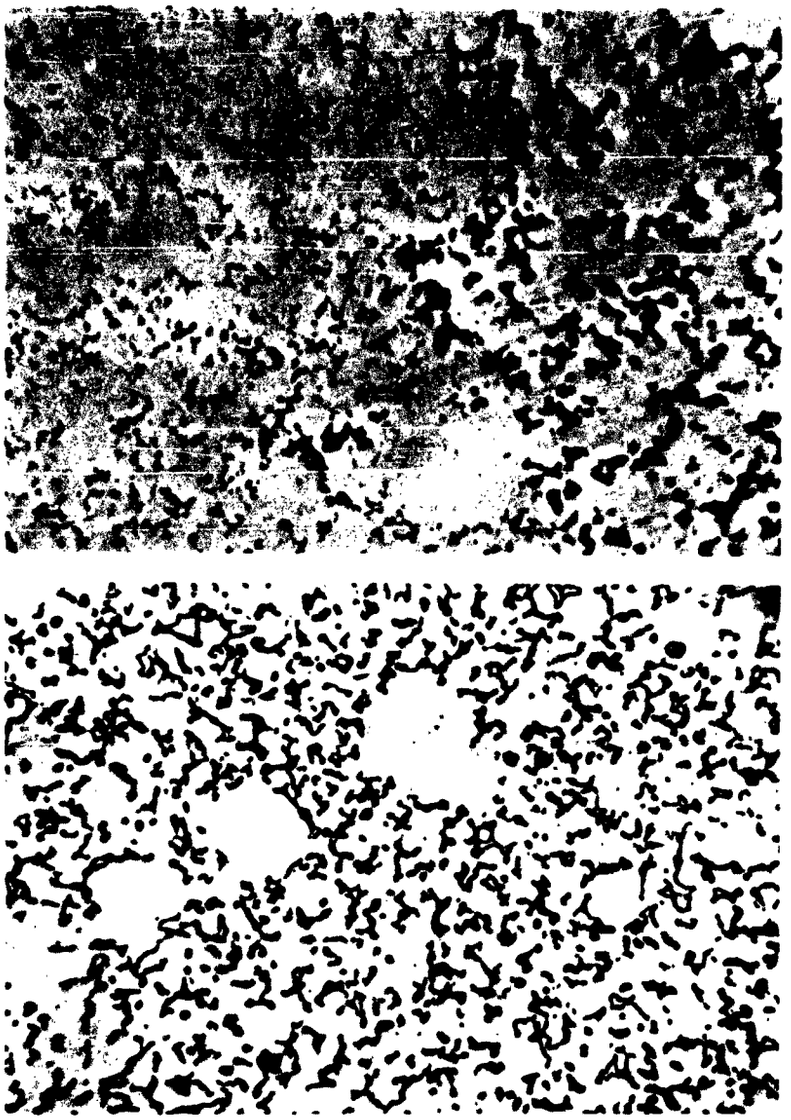

Fig. B8 – Interparticle "porosity" in section A of insert B-1 (CP-4 etch) 500X. (a) Adjacent to Al_2O_3 infiltrated region, (b) Interior of uninfiltrated region.

concentrations of this porosity. Since it has been demonstrated that the CP-4 etchant will delineate carbides, the structures revealed by this etch in Figs. B8a and B8b may indicate fine carbide particles along the tungsten particle boundaries. A specimen showing a high concentration of this structure was selected and analyzed for carbon (combustion analysis). The carbon content was 0.05 wt-%. Unfortunately the solubility of carbon in tungsten has not been determined accurately and thus it is impossible to decide whether carbides should be present in this material. If zero solid solubility of carbon is assumed, the 0.05 wt-% C would produce 1.5 to 2 vol-% of W_2C. Thus, it is possible that carbide films, formed during the pressing and sintering operations may have

impaired the bonding of the tungsten particles and produce the observed structures. However, the present data and observations are insufficient evidence to conclude that carbon, as carbides, has a role in defining this structure.

Cracks

Aside from erosion, crack formation in the nozzle inserts, presumably attributable to differential thermal expansion during firing, represents the major deterrent to the successful use of tungsten in this application. The variation in the susceptibility to cracking of two similar parts subjected to very similar tests is illustrated by a comparison of these two inserts. Since insert B-1 was badly cracked in the test, and the fillet area beneath the entrance collar contained a large number of cracks, it would be natural to attribute this concentration of cracks to the change in heat flow and the stress concentration produced by the change in section thickness. As a logical extension of this, the B-2 insert should have been more susceptible to cracking because the design change reduced the radius of the fillet alone. In test, however, this insert developed very few cracks. The reason for this rather anomalous behavior is probably to be derived from the difference in the structure of these two inserts of "similar design and manufacture".

Cracks Originating in the Contaminated Areas – Although the second phases appearing in the contaminated areas along the entrance surfaces and the exit ends of these two inserts were different, the nature of the cracks generated in these two areas is the same. The microstructures of both areas (see Figs. 5 and 6) indicate that a liquid phase formed during the test firing. Based on the identifications of these second phases, this requires that the temperature of the entrance surface exceeded 2475°C (4485°F) (the binary W + W_2C eutectic temperature) and the exit, 1640°C (2985°F) (the binary peritectic generating the zeta phase). All reasonable estimates of the temperatures to be expected in the inserts during the firing exceed these liquation temperatures. The cracks found in these regions are probably formed by hot tearing during the cooling of the inserts after testing. This conclusion is supported by the observations that the cracks are confined to the affected areas and that the cracks are only partially filled with Al_2O_3 (Figs. B3 and B6).

In these inserts, this cracking is not detrimental to the performance of the nozzle. The source of the contamination, and hence the cracking, at the exit is known and presumably can be avoided. The deterioration of the entrance surface, though not damaging in these tests, should not be ignored. In these inserts the erosion of the entrance surface was slight, but if the extent of the contamination had been greater, portions of this surface may have been deeply eroded and the inserts may not have survived the test. However, there is some reason to believe that this contamination may occur late in the test. The entrance surface of both B-1 and B-2 displayed a number of pits, but none was extensively eroded and none had developed an extensive contaminated zone beneath it. In addition, the contaminated region on B-1 shown in Fig. B3a has not impaired the infiltration of aluminum oxide through this area. If the contamination had occurred early in the test, the liquid phase formed by this process might have formed an effective seal to inhibit the alumina infiltration.

Circumferential Cracks – Whiel B-2 contained only a single circumferential crack, B-1 contained a series of cracks. In the region of the fillet, a large number of the cracks were predominantly of the circumferential type. These cracks probably formed late in the test and may actually have been formed during the cooling of the insert after the test. This conclusion appears justified since there was little flow of Al_2O_3 into the cracks shown in Fig. B3. Thus these cracks must have penetrated into the alumina infiltrated region after the supply of this oxide was exhausted.

The surfaces of the fillet crack of Fig. B3a were coated with tungsten carbide. Figure B9, a photomicrograph of an area near the terminus of this crack in the alumina infiltrated zone, shows that may of the pores in the very porous region around the crack are lined with carbide and filled with Al_2O_3. The crack itself is almost entirely empty. From these observations it is logical to assume that the crack reached this depth before the alumina had penetrated the region from the opposite face. The heavy coating of carbide indicates that the carbon back-up block was hot and giving off the carburizing gas at that time. The lower crack, Fig. B3b, did not show a carburized surface in this section. However, by exposing the crack surfaces and examining them on the x-ray spectrometer, carbides were detected. A study of the

Fig. B9 — Carbide layer on tungsten along the fillet crack of Fig. B3a (CP-4 etch) 500X

crack surfaces by electron microscopy showed that this crack had formed by plastic intergranular decohesion.* This mode of fracture was observed even at the outer surface, indicating that the outer surface was "hot" when the fracture was initiated. The failure to detect the carbide layer by metallographic means may indicate that coverage was spotty or that the layer is very thin. The x-ray data appear to support the latter conclusion and thus indicate that this crack may have formed very late—perhaps when the part was cooling.

Longitudinal Cracks—The two longitudinal cracks in positions E-F of Fig. B2 are shown in a section normal to the throat axis of B-1 in Fig. B10. These two cracks, enveloped in clouds of exaggerated porosity in the uninfiltrated region of the insert, can be traced in this section from the outer surface, across the uninfiltrated region, and deep into the Al_2O_3 filled region around the throat. Within the infiltrated region and in some portions of the uninfiltrated region the cracks appear as very fine lines. Two examples of this structure are shown in Figs. B11a and B11b. Figure B11a shows the trace of the lower crack in Fig. B10 crossing the innermost portion of the uninfiltrated region and entering the Al_2O_3 filled region. Figure B11b shows a section of the upper crack of Fig. B10. This area is located near the outer surface but, again, the crack appears as a very fine line. These observations indicate that these longitudinal cracks in insert B-1 were formed

*This mode of fracture has been observed in other tungsten nozzle inserts. See NRL Memorandum Report 1217 by E. P. Dahlberg of Sept 1961.

Fig. B10 – Transverse section of B-1 containing two longitudinal cracks along position E to F, below fillet (CP-4 etch) 8X

very early in the test firing, that the cracks penetrated almost to the throat surface, and that as the insert was heated and expanded the restraint of the back-up block placed the insert in compression and forced these cracks to close. The fine traces of the cracks shown in Fig. B11 represent the healed sections of these cracks.

Carbide contamination along these cracks was limited to a narrow region near the outer surface. This suggests that the cracks were forced closed before the carbon backup block became very hot. Thus, the formation of the longitudinal cracks and the subsequent partial repair of these cracks occurred very early in the test of the insert.

Although no evidence of longitudinal cracks was observed on the outer surfaces of insert B-2, fine traces, indicative of healed cracks, were found in transverse sections of this insert. These traces, while less well defined than those of B-1, indicate that this insert had also fractured during the early moments of its test.

In Fig. B10, a few short cracks can be seen along the surface of the throat. These cracks probably formed during the cooling of the insert after the test and thus were not detrimental to the performance of the nozzle.

POROSITY

The nature and distribution of the porosity in insert B-1 is varied and complex while the porsity in B-2 is much more uniform. These differences are evident in the dark-field macrographs of Figs. B3 and B4. A question of great importance in defining the required characteristics of nozzle insert materials is whether the primary cause of the very different susceptibility to cracking observed is due to porosity differences that existed in the inserts before test firing. Unfortunately, there appears to be no known way of examining the porosity distribution in pressed and sintered blanks of 70 to 80 percent density by nondestructive tests. If the difference in porosity distribution in these two inserts is a consequence of the test firings, then the important question is why the structures of these two inserts of very similar manufacture and test history should show this great difference. With this lack of information or confidence in the stated information on the initial state of the inserts, any explanation of the generation of porosity in some sections or, the elimination of porosity in other is conjecture. The description of the porosity that follows will show that the problem is unclear.

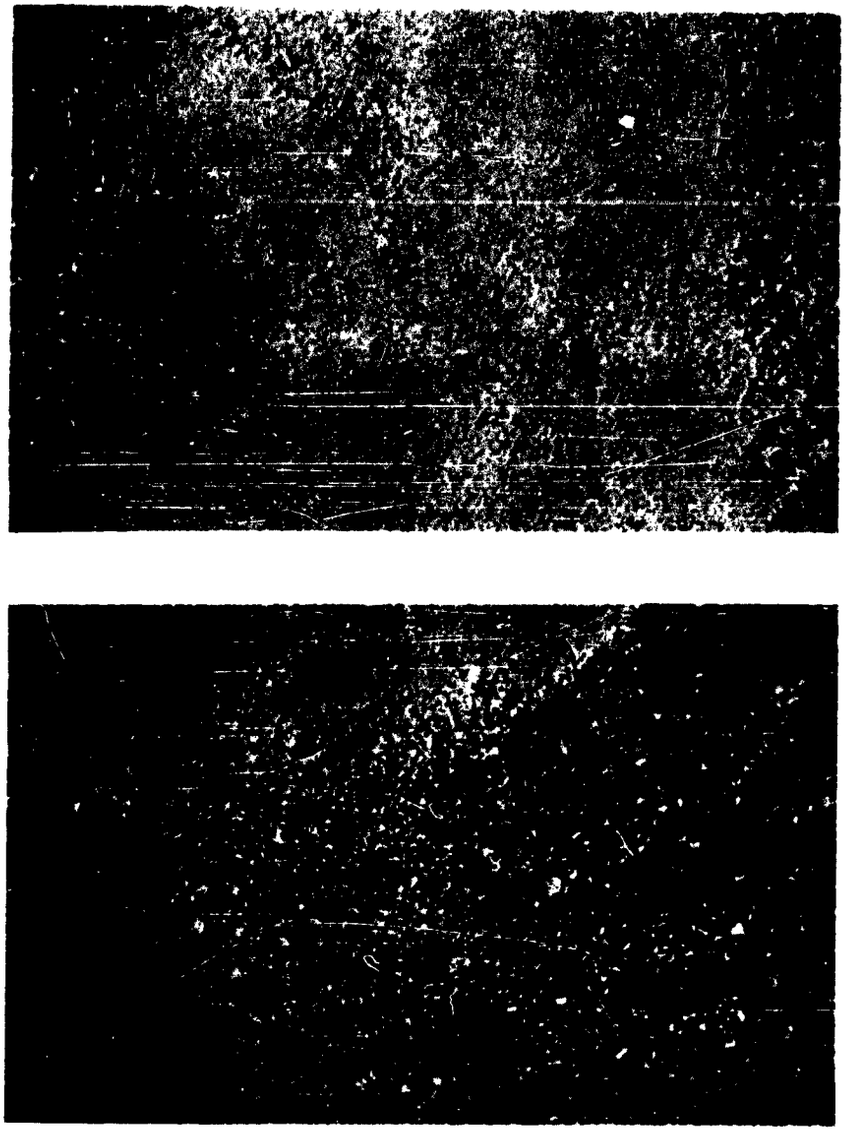

Fig. B11 – "Repaired" sections of longitudinal cracks shown in Fig. B10 (CP-4 etch) 55X. (a) Crack trace across dense region and in Al_2O_3 filled region (lower crack of Fig. B10). (b) Crack trace near outer surface (upper crack of Fig. B10).

The nature of the porosity associated with cracks in these inserts has been illustrated in Figs. B3 and B10. The circumferential crack originating in the fillet section of Fig. B3a shows an envelope of exaggerated porosity of considerable thickness. The broadening of the porous region below the crack may be caused by other cracks in the vicinity of this section since there are many cracks in this region. The zone of enlarged porosity around the circumferential crack near the exit, Fig. B3b, is so thin that it is not visible at this low magnification. This crack, forming late in the test, has been shown to open by a plastic decohension mechanism. The deformation of the region around the crack could thus account for the enlarged porosity that is observed.

The longitudinal cracks appear to form very early when the material is cold and not deformed easily. These, however, are surrounded by extensive regions of enlarged porosity as seen in Fig. B10. Since deformation of this large volume of material is unlikely, there appears to be no ready explanation for the generation of these pores unless their presence in the initial blank is assumed.

As noted in an earlier section of this report, the pores infiltrated with alumina were larger and of simpler form than those in the adjacent uninfiltrated material. Since the hard oxide filling of these pores facilitated the preservation of their true section sizes in the polished specimens, it was possible to determine the percent porosity in the infiltrated regions of these two inserts by the well established quantitative metallographic technique of point counting. Three areas were measured on each of the inserts—one close to the throat surface, one midway in the infiltrated region, and one near the outer surface of the region. The percent porosity in each of the areas was determined as 15 to 19 vol-% or 85 to 81 vol-% tungsten. This is identical with the specified density of the pressed and sintered tungsten blanks from which these inserts were machined. Thus, within the alumina infiltrated regions of inserts B-1 and B-2 there has been no change in the volume of the pores. The distribution of the pores may have changed but their total volume is the same as that specified for the average of the initial material.

For insert B-2, where the infiltration was complete and the measurements of the pore volumes covered the entire thickness of the piece, this means that no change in the density of the tungsten packing occurred during the test of the insert. The uniformity of the porosity is shown in Fig. B4 and there is little or no evidence of densification of the structure by upsetting along the throat or in the body by the compressive forces derived from the temperature gardient or the restraint of the carbon backup block.

The significance of the non-uniform distribution of the porosity in insert B-1 remains unresolved. It seems impossible to reconcile the observations that the longitudinal cracks penetrate deeply into the now infiltrated region, and that the porosity within this infiltrated region is uniform, with the predicted upsetting of the throat and the movement of a compression wave through the insert wall. If the longitudinal cracks had stopped short of the inner boundary of the high density region, then the observations would suggest the interruption of the compression wave by the formation of these cracks. This, however, is not the case. Similarly, it is quite difficult to imagine that the observed abrupt change in porosity across the smooth interface of the infiltrated zone was produced during the pressing and sintering of the tungsten blank. The shape of the low density region along the entrance and throat of the insert does bear some slight resemblance to the zones of compaction one might expect to find if the powder were pressed around a central mandril in a single acting die.

SUMMARY

These two sub-scale rocket nozzle inserts of similar design, machined from the same lot of pressed and sintered tungsten blanks, and subjected to identical test firing conditions have shown obvious dissimilarity in cracking and alumina infiltration susceptibility. Examinations of the external surfaces of these inserts would appear to indicate that B-2, the insert showing only one circumferential crack and also the insert which was completely infiltrated with Al_2O_3, was superior to B-1. The test firing performance data, however, indicated that both inserts were equally good. Detailed examinations of the inserts after test have also shown that the damage incurred during the tests in these two inserts was rather similar.

The type of contamination damage on the entrance and exit surfaces of both inserts was very similar. The pitting of the entrance surfaces and the associated hot tearing at these sites appear to be caused by carbon contamination. Since these cracks are probably formed in the cooling process after the test, they are not considered to be damaging. More extensive contamination of this surface may, however, lead to damaging erosion at these sites. The erosion, or spalling, and cracking at the exit end of these inserts were caused by contamination arising from the melting of a part of the steel motor closure. This can be avoided and is thus not considered in evaluating these inserts. The carburization of the external surfaces of both parts by reaction with the carbon back-up block has not appeared to impair their performance.

The finding that the longitudinal cracks almost penetrated the entire wall thickness indicates

that these cracks formed very early in the test. Although traces of this type of crack were not observed on the external surface of insert B-2, evidence of these deep cracks were found in sections of this insert. Thus, both inserts had been cracked by the stresses produced in the early moments of the firing. The formation of such deep cracks must greatly weaken the insert. However, the number of cracks is small and in thick walled inserts such as these the "keystone" effect may prevent this damage from destroying the nozzle. In thin walled inserts the formation of cracks of this type may result in the ejection of the nozzle. Thus, it is possible that the improved performance of the current full scale inserts is attributable to both improved material and to the design change.

The fact that the surfaces of the longitudinal cracks were not carburized and that portions of the crack had healed suggests that these cracks were forced closed soon after they formed. It seems likely that the restraint of the insert mounting members against the expanding insert is responsible for this partial repair. In general, the rigidity of the insert mount has been ignored in calculations of the thermally induced stress system in the insert. These observations suggest that the restraint of the mount may not be negligible in these calculations and the design of the insert and the mounting.

The type of fracture and the formation of tungsten carbide on the fracture surfaces of the circumferential cracks indicates that they were formed after the insert had been heated and before the insert and carbon back-up block had cooled. Thus, they could have been formed as early as a few seconds after the ignition of the propellent or as late as during the cooling period after the test. If they were formed during the cooling period then the larger number of these cracks in B-1 than in B-2 is of no importance. If they formed early in the test, then this difference in cracking may be of importance but neither the time of formation nor the effects of this type of crack on the performance has been established. Thus the evaluation of this type of defect must await the results of future tests in this series—tests designed to measure strains at the outer surface of the insert during the firing.

The differences in the distribution of porosity in these two inserts appears to account for the differences in the infiltration of these structures by molten alumina during the tests. The porosity distribution in B-2 was rather uniform and the entire insert was infiltrated with alumina. The pore volume in this insert after the test was identical with that specified for the original pressed and sintered blanks of tungsten. The region around the throat of B-1, which was infiltrated with alumina also, had a pore volume approximating that of the original material. The porosity in the remainder of this insert, however, was very non-uniform and on the average substantially below that specified for the material. These observations indicate that the non-uniform pore distribution in B-1 may have existed in the pressed and sintered blank from which it was machined. This difference, however, should have been large enough to have been detected in the calculation of the density of the blank from its mass and volume. The shape of the region of high porosity in this insert bears some resemblance to that expected if a single acting die were used in compacting the powder around a central mandril. It is unlikely that this method of compaction was used, but since no information on the manufacture of the blanks is available, this possibility cannot be ignored. However, as indicated above, the real difference in the damage incurred by the two inserts in these tests is in the number of circumferential cracks found in the parts after the tests. Since the time at which these cracks formed during the test cannot be determined, there is no real evidence to indicate that the more uniform distribution of porosity and the lower density of insert B-2 makes it a more desirable type of material for inserts of this design.

APPENDIX C
METALLOGRAPHIC AND FRACTURE STUDIES OF INFILTRATED TUNGSTEN INSERTS

R. A. MEUSSNER
Physical Metallurgy Branch
Metallurgy Division

INTRODUCTION

While it has not been feasible to conduct extensive studies of the large number of nozzle insert specimens in this series of experiments, an analysis of two representative specimens has provided some additional evidence of the characteristics of this class of materials. Since the observations presented here are from a very limited sampling of the total number of specimens, the importance of some of the observations may be weighed too heavily. However, these observations suggest interpretations which may be of use in furthering the understanding of the response of these materials to thermal cracking.

THE SPECIMENS

The two nozzle inserts shown in Fig. C1, from early tests in this series, were selected for comparison and study. With the exception of the differences in the infiltration procedures (B-5 was infiltrated with copper and B-6 with silver), the manufacture and testing of these two inserts were intended to be identical. Both had been prepared from the same lot of tungsten powder and pressed and sintered to 80-percent-density blanks by the same manufacturer. Both blanks were infiltrated by another manufacturer, ultrasonically inspected, machined to nozzle inserts in the same laboratories and shops, and finally test fired under the same conditions. While the pressure and temperature traces from these two tests indicated that the conditions were very similar and both inserts survived the tests, an examination of the inserts after the firing revealed that B-6 (Ag) had formed a crack at the root of the circumferential notch while B-5 (Cu) showed no cracks. Although the extent of the crack in B-6 (Ag) is not shown clearly in Fig. C1 (it extends more than halfway through the insert wall), its location is quite evident.

Pieces of several other infiltrated tungsten bodies were examined to provide comparative data. The known histories of these, as well as B-5 and B-6, are collected in Table C1. The portion of the full-scale nozzle insert, AGC (Ag), was from a successful static motor test conducted at the Aerojet-General Corporation facility in October-November 1962. This material is probably also representative of the class of infiltrated material employed in the A.R.C. tests. The last four specimens of Table C1 represent unfired samples of infiltrated materials. However, these were of different manufacture than the nozzle inserts and thus a direct comparison may not be entirely objective. Unfortunately, no unfired specimens of material equivalent to B-5 (Cu) and B-6 (Ag) were available for this study.

TEST RESULTS

The results presented in the other sections of this report and summarized in Figs. A1 and A2 of Appendix A clearly indicate the superiority of the copper infiltrated material. For the purposes of this section, only the data from the 80-percent-density infiltrated specimens will be considered. If it is recognized that thermal cracking occurs only at the outer "cold" surface and the short laminar cracks found near the inner hot surface have some origin other than thermal cracking, the data of the first two classes (no cracks and only short laminar cracks) can be combined to give a sufficiently large number of observations for comparison. These data show a very much smaller incidence of both thermal cracking and laminar cracking in the copper infiltrated inserts than that observed in those infiltrated with silver.

INSERT MICROSTRUCTURE

A comparison of the structures of inserts B-5 (Cu) and B-6 (Ag) is shown in the photographs and diagrams of Figs. C2 and C3. B-5 (Cu) shows no evidence of thermal cracking while B-6 (Ag)

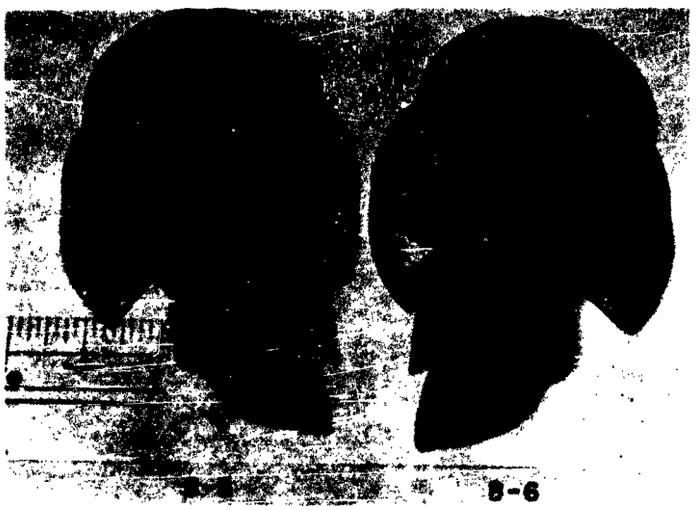

Fig. C1 – Infiltrated nozzle inserts sectioned after test firing, viewed from exit end. The thermal crack is visible at base of the circumferential notch in the section of B-6 (Ag).

TABLE C1
Description of 80%-Density Tungsten Infiltrated Materials

Specimen Designation	Infiltrant	Manufacturer*		Test History
		Body	Infiltrant	
B-5	Cu	GE	M	Atlantic Research Corporation
B-6	Ag	GE	M	Atlantic Research Corporation
AGC	Ag			Full scale test, Aerojet-General Corp. Nov. 1962
50W3	Cu	M	M	Infiltrated nozzle blank – no firing
5S	Ag	M	M	Infiltrated nozzle blank – no firing
1H	Cu			Notch bend specimens
1B	Ag			Notch bend specimens

*GE – General Electric
M – Mallory

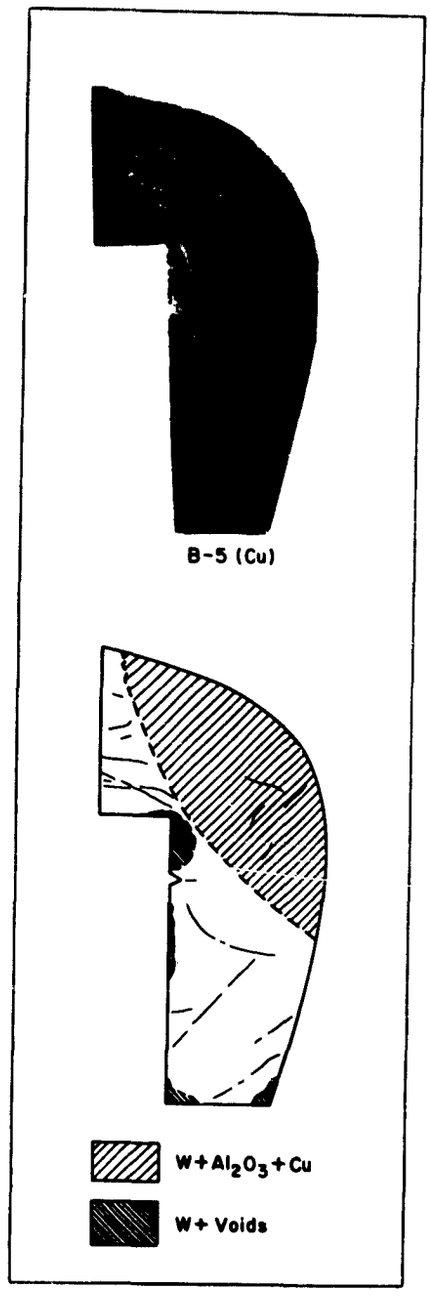

Fig. C2 — Photomacrograph and diagram of B-5 (Cu) showing extensive alumina penetration, slight evidence of cellular structure, and no thermal crack (Mag 3X)

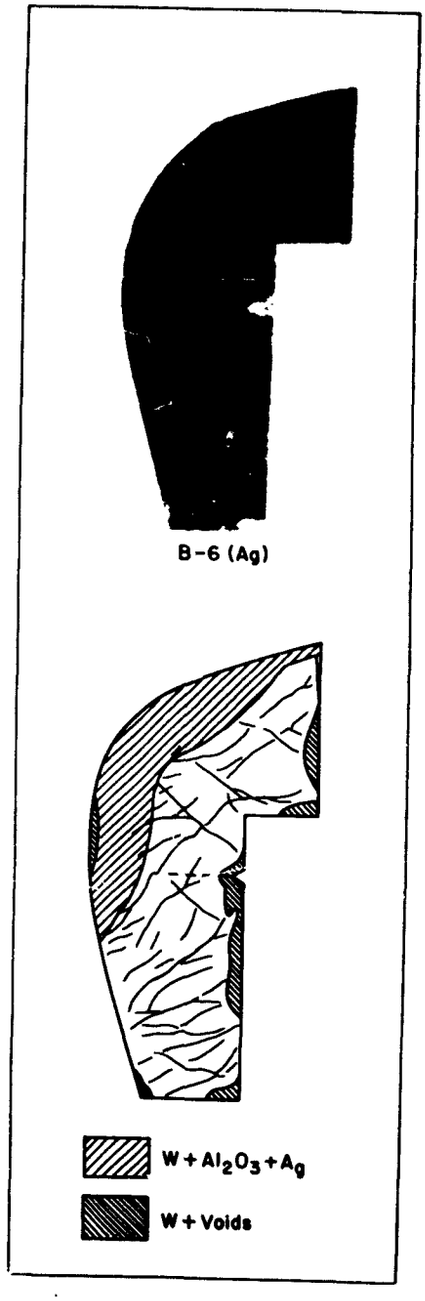

Fig. C3 — Photomacrograph and diagram of B-6 (Ag) showing more limited alumina penetration, a pronounced cellular structure, and a deep thermal crack (Mag 3X)

shows a crack extending a little more than halfway through the insert wall. In view of the distinction between thermal cracking and laminar cracking indicated above, these are representative of thermal cracking in these two classes of materials. The absence of laminar cracking along the inner surface of this section of B-6 (Ag) is not representative. Selection of a sectioning site to reveal thermal cracks is rather simple since these cracks are generally visible on the outer surface of the insert, particularly when notches have been added to provide preferential sites for their formation; however, laminar cracks formed along the inner surface are seldom detectable on the insert surface. While the section shown in Fig. C2 does not contain laminar cracks, other sections of this same insert should reveal their presence. As seen in Table C2, five of six such sections of this type of material showed laminar cracks.

Both B-5 (Cu) and B-6 (Ag) showed a thin coat of tungsten carbides at some sites along their outer surfaces and some areas along these surfaces where contamination had occurred from the ceramics used to support thermocouples and strain gages. The inner surface was covered with the usual spatter of alumina and carbonaceous material from the flame, and a region saturated with alumina borders this surface. The depth of this alumina infiltrated region was much more extensive in the copper than in the silver infiltrated material. Within the regions penetrated by alumina, from 40 to 70 percent of the original metallic infiltrant was lost during the test firing and most of this volume was occupied by alumina. Variations in the coloration of these zones in Figs. C2 and C3 is caused by variations in pore and alumina particle size and in the amount of metallic infiltrant replaced by alumina. With the exception of a number of small pockets, generally along the outer surfaces of the inserts, where the metallic infiltrant was lost and no alumina replaced it, a very large part of the original metallic infiltrant remained in the unaltered body of both inserts. In these two sections it appeared that there had been a greater loss of copper than of silver. Since this appears to be a general observation for the inserts of these tests, it indicates that the boiling point of the metal is not rate determining in the mechanism of infiltrant loss.

The pattern of fine irregular lines which show clearly in the photograph of the section of B-6 (Ag) in Fig. C3 is another characteristic of this material. The pattern of these lines in B-5 (Cu) and B-6 (Ag) is indicated in the accompanying sketches and here it is evident that the number of these lines is much greater in the silver than in the copper infiltrated material. Examination at higher magnifications showed that these lines were very thin zones of rather low pore density. As a consequence they were more resistant to grinding than the body of the insert and could be made prominent in the structure by overpolishing to leave these thin zones in relief. Within the zone penetrated by alumina this effect was minimized by the abrasion resistance of the alumina. Thus the apparent absence of these lines in the regions containing alumina reflects the difficulty of detecting these lines rather than a real change in the structure of these regions. The difference in the number of lines found in the body of the silver and copper infiltrated inserts, however, is real and may explain the difference in incidence of laminar cracking in these two types of inserts.

Figure C4a shows some of these thin dense zones in the vicinity of the thermal crack of B-6 (Ag). Since these lines appear to cross the crack path it seems reasonable to conclude that they were present before the crack was formed. Thus these lines must have been present in the infiltrated insert before the test, for the thermal crack is known to form very early in the firing test. The true nature of the lines observed in these sections was revealed by polishing two surfaces, approximately perpendicular to one another, on a piece of the exit portion of B-6 (Ag). Figure C4b shows that the lines on a radial plane of this insert are continuous with lines on a plane parallel to the throat face. These lines are in fact warped surfaces dividing the insert into irregular cells.

This type of cellular structure in the silver infiltrated inserts of these tests may explain the high incidence of laminar cracking observed near the hot inner surface. Since the tungsten bodies were successfully infiltrated it is obvious that these cells were interconnected during this process. In the thermal conditions of a firing test, however, melting of the infiltrant metal will occur progressively within the volume of each cell. Under these conditions the normal exit channels for the liquid metal may remain frozen while a high hydrostatic force is generated by the volume increase of the melting metal. In this way the cell wall may confine the liquid and cause the tungsten structure to

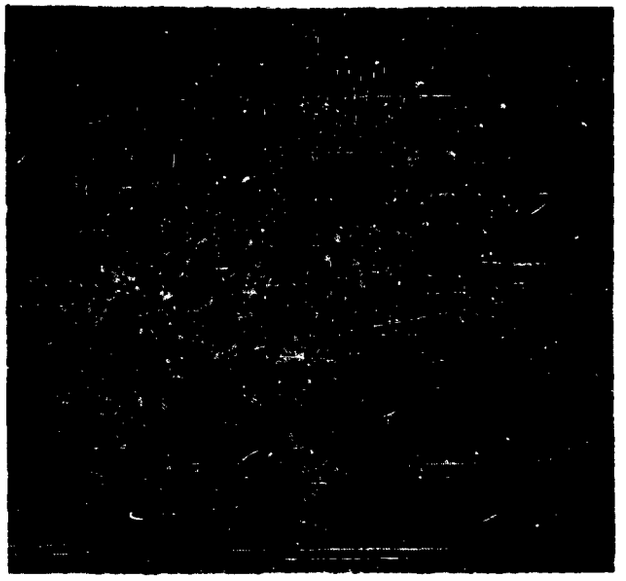

(a) Thin dense tungsten zones in the vicinity of the thermal crack (Mag 50X)

(b) Edge view of specimen from the exit portion showing the matching of traces of the dense zones on two surfaces (Mag 8X)

Fig. C4 – Cellular structure in B-6 (Ag)

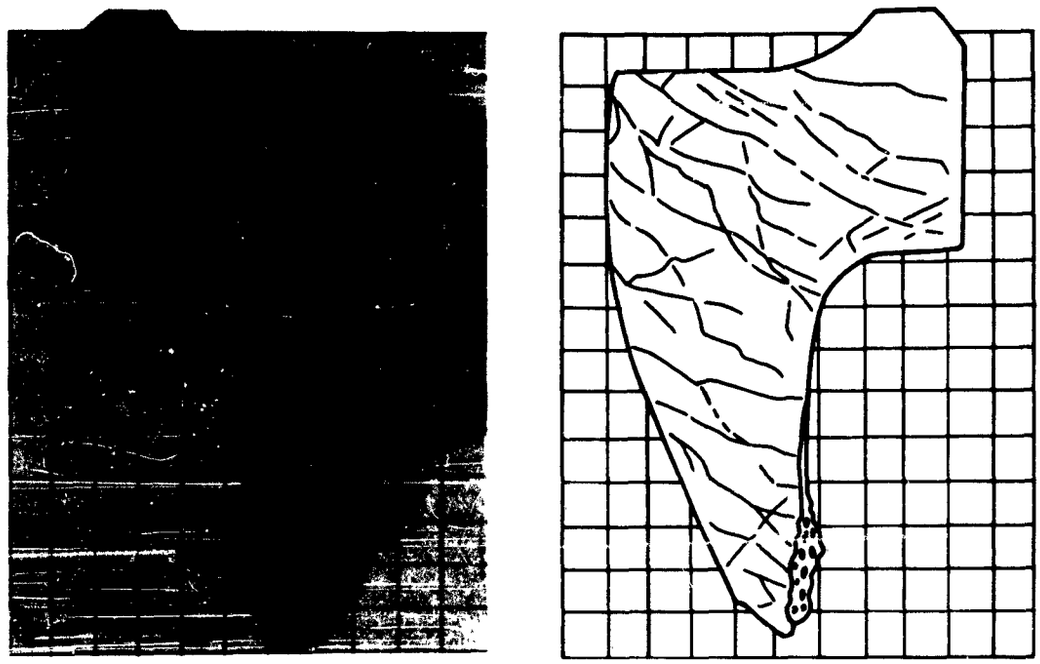

(a) Transverse fracture surface formed at, or near, room temperature

(b) Pattern of cellular structure observed on section approximately 3/8 inches below fracture of Fig. C5a

Fig. C5 — Portion of silver infiltrated nozzle insert from a full-scale static firing test AGC (Ag)

rupture forming a laminar crack. This can happen most readily near the inner surface since there the restraining tungsten structure is thin and already weakened by the rise in temperature and the high heat flux and steep temperature gradient should accentuate this effect.

As has been indicated, the origin of this cellular structure is not clear. Examinations of other infiltrated tungsten bodies which had not been subjected to the temperature cycle of a firing test failed to reveal any marked evidence of this type of structure. These parts, 50W3 (Cu), 5S (Ag), 1H (Cu), and 1B (Ag), however, were of different manufacture than the inserts B-5 (Cu) and B-6 (Ag). As shown in Fig. C5, a section of a full-scale nozzle, AGC (Ag), did show this same type of cellular structure. The conditions of manufacture of this part, however, are unknown. The present observations indicate that this cellular structure (a) may be formed during the firing tests, although this is considered unlikely since the cell walls cross the thermal crack, (b) may be formed in the infiltration process, although this also seems unlikely and no details of these processes are available, and (c) may be formed in the original loading of the powdered tungsten into the die for compaction. The cellular structure is suggestive of the type of segregation of particle sizes that might be expected if the die were loaded incrementally. However, since it seems unlikely that the manufacturing process was altered to remove this effect during the processing of the blanks used for the two groups of inserts for these tests, the origin of this structure remains unclear.

Since the nature of the cellular structure has been established, its effect on the fracture path was examined. A comparison of the cellular structure and the fracture surface of AGC (Ag) in

Fig. C5 suggests some interdependence. A detailed examination of this surface revealed a number of ridges which were directly attributable to the cell walls. From the small amount of oxide on this fracture surface it is clear that it formed late in the cooling process after the firing test, and thus this surface represents a fracture formed near room temperature. Room temperature fractures of portions of B-6 (Ag) also showed ridges associated with the cell walls. However attempts to examine fractures in the cell walls by electron microscopy have been unsuccessful, presumably because the fracture through the wall is not greatly different from that in the bulk of the material. The observation that the thermal crack formed in B-6 (Ag) was not diverted by the cellular structure appears to support this conclusion.

FRACTURE SURFACES

Since the strain gage measurements have decisively confirmed that thermal cracking occurs at the outer surface of the nozzle insert while this surface is still at a low temperature—a few hundred degrees Fahrenheit above ambient; room temperature fractures of unfired material should reveal the same structure as that formed at the initiation of these fractures in a nozzle. To examine the fracture mode in these rather unique structures containing a continuous skeleton of tungsten within a continuous matrix of a ductile, though severely restrained, infiltrant metal, plastic replicas were prepared from room temperature fracture surfaces of 1-H (Cu), 1-B (Ag), B-5 (Cu), and B-6 (Ag). These replicas, shadowed with Pd and backed with evaporated carbon films before the plastic was dissolved, were examined at moderate magnifications in an electron microscope.

The fracture surfaces of the infiltrated materials 1-H and 1-B are represented by the structures of Fig. C6. To provide positive identification of the infiltrant metal in these fracture replicas a specimen of 1-H (Cu) was held for 10 minutes at 110°C in air, thus selectively oxidizing the copper surfaces. In the electron micrograph of the replica from this specimen, shown in Fig. C6b, the unoxidized tungsten surfaces are clearly defined. Similar tungsten surfaces are evident in the fractures of 1-H (Cu) and 1-B (Ag) shown in Figs. C6a and C6c respectively. The smooth, often rather round, areas represent the fracture of tungsten tungsten grain boundaries. On these surfaces some small impurity phase particles, probably carbides, are often visible. The other tungsten surface, prominent in Fig. C6b, shows a typical river pattern indicative of cleavage. Thus these areas represent the fracture of individual tungsten particles. Since these electron micrographs represent a very small sample of the total fracture surfaces, they were selected to provide examples of specific structural features and none portrays the average character of the fracture surfaces in these materials. In both the copper and silver infiltrated materials, failure of the tungsten skelton by grain boundary separation and by cleavage was observed, and in both materials grain boundary separation was predominant.

The copper or silver surfaces in these fractures are, in general, smooth and featureless and appear as a puckered fabric dividing the area into a number of cells centered on the individual tungsten surfaces. As indicated in the oxidized specimen (Fig. C6b), there is very little stripping of the copper from the tungsten particle surfaces in the fracture process. However, in the fracture of the silver infiltrated specimen (Fig. C6c), some of the silver surfaces bear the imprint of a pocked surface. While the positive identification of the origin of this feature of the structure would involve a rather exhaustive study it seems reasonable that such marking could arise by the separation of the silver from the surfaces of unfractured tungsten particles. Such separations may be facilitated by impurity phases coating these particles, or by small voids formed by incomplete infiltration, or by the rejection of dissolved gases during the solidification process. In any event, these markings present in the silver were not observed in the copper infiltrated material. The above interpretation of these markings would appear to provide an additional low energy separation mode for the silver that is not operative in the copper.

The fracture mechanism for these materials under isothermal conditions at room temperature is schematically illustrated in Fig. C7. Although the infiltrant is constrained by the geometry of the system, the major portion of the load is borne by the rigid tungsten matrix. As the load is increased, some of the weaker tungsten grain boundaries separate and these failures lead to a progressive and rapid fracture of the remaining

(a) 1-H (Cu)

(b) 1-H (Cu) - copper selectively oxidized in air

(c) 1-B (Ag)

Fig. C6 — Electron macrographs of infiltrated specimens fractured at room temperature

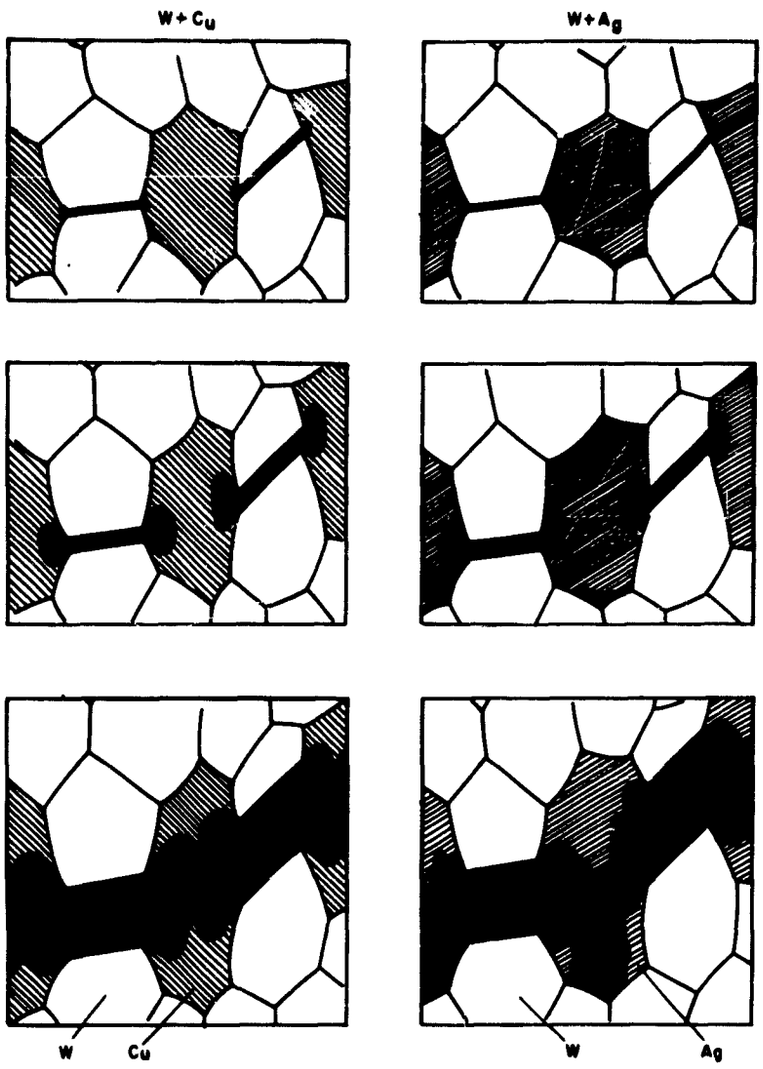

Fig. C7 – Schematic of fracture mode in copper and silver infiltrated tungsten

tungsten structure either by grain boundary separation or by cleavage of individual grains. During this process the load is shifted to the infiltrant metal and the individual cracks initiated by the fracture of the tungsten grow in the infiltrant and produce the dimpled rupture surface observed in the accompanying figures. This type of failure has been observed in other comparable materials (*i.e.*, wrought iron as studied at NRL, and several eutectic structures as studied by Hertzberg at United Aircraft). As shown rather clearly in Fig. C6a each of the tungsten fractures generates one large dimple and because of the extensive stretching of this surface it appears quite featureless. In the fracture of the silver infiltrated material, the separation of the silver from the tungsten curtails this stretching process. This effect may explain the order of merit ratings obtained in the notch bend studies reported in the first part of this report (*i.e.*, silver infiltrated material is intermediate to the uninfiltrated and the copper infiltrated tungsten).

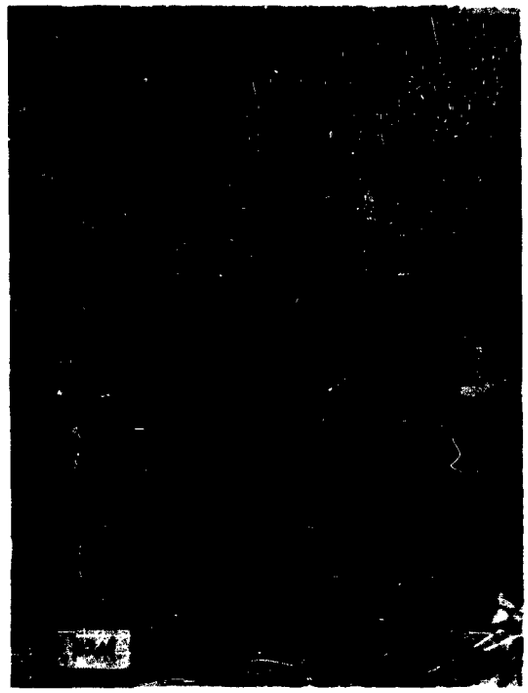

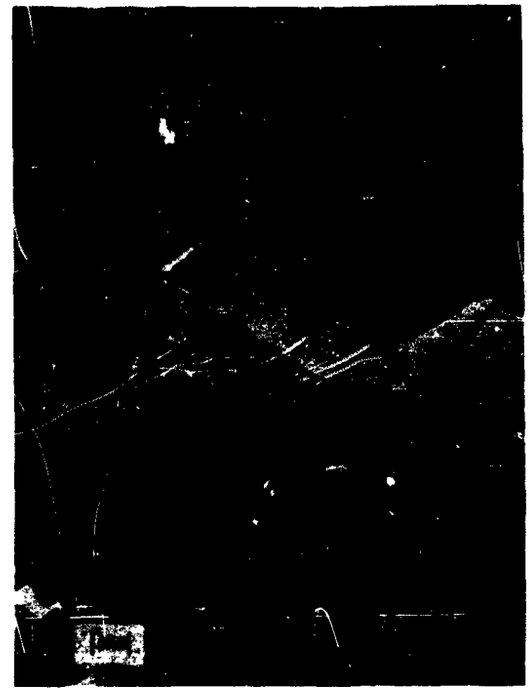

Fig. C8 – B-5 (Cu) – specimen from outside the major zone of alumina penetration

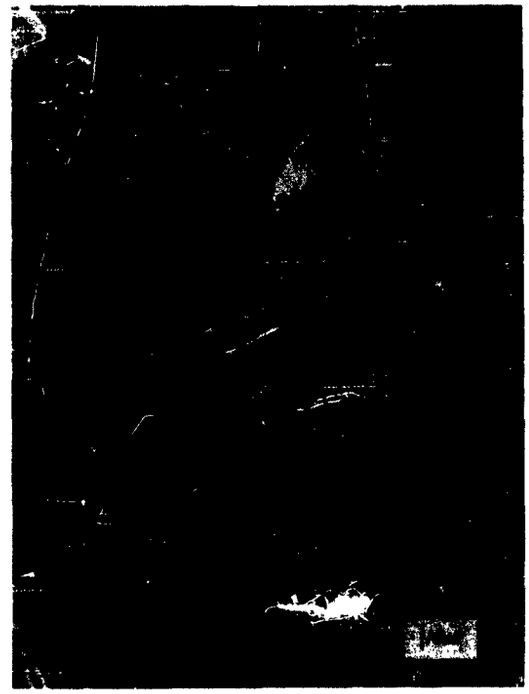

Fig. C9 – B-6 (Ag) – specimens from a region containing alumina

The interpretation of electron micrographs of fractures in nozzle insert materials after test firing is much more difficult, for the insert may now contain extensive voids; infiltrant metal; oxides of the infiltrant, tungsten, and aluminum; carbides; and a variety of mixed phases of these components. Only a few representative structures are included in this report (Figs. C8 and C9). These show regions of fracture surfaces in B-5 (Cu) and B-6 (Ag) produced by breaking samples at room temperature. The larger particle size of the tungsten used in the manufacture of these inserts is at once obvious. In all three of these structures the tungsten has failed by cleavage and by grain boundary separation, and it may be noted that the population of impurity particles on these surfaces is not significantly higher than that observed in the infiltrated material of 1-H and 1-B. In Fig. C8, dimpled rupture of the remaining copper is again evident. The large rough surface at the top of this figure has not been identified. It may be an oxidized surface of tungsten. Figure C9 illustrates the structure of the

silver infiltrated insert near the throat surface. The large areas showing chevron or cleavage step markings are probably fractures in the alumina. Some silver showing the dimpled rupture pattern is visible, and in a few areas tungsten or silver surfaces were observed to show marking similar to the imprints found on the silver of Fig. C6c. The large rough area in the center of Fig. C9b has not been identified. However, this area is bounded by dimpled silver along its lower boundary. Thus it may be a complex oxide mass or perhaps a contaminated silver phase.

Summary

The superior performance of the copper infiltrated tungsten specimens in the thermal shock tests of the small motor firings and in the notch bend tests is supported by these metallurgical observations. While the silver infiltrated material employed in the small nozzle tests displayed an unusual cellular structure, the present evidence does not indicate that the inferior thermal crack resistance of this material can be directly attributed to this structure. The evidence does suggest that this cellular structure may be responsible for the high incidence of laminar cracking near the inner surface of these nozzle inserts.

Fracture surfaces produced at room temperature are assumed to be representative of the initial fractures occurring at the outer surface of the nozzle inserts during a test firing. This is a reasonable assumption since it has been shown that the thermal cracks form before the temperature at this surface has increased by more than a few hundred degrees Fahrenheit. Studies of these surfaces provided a model of the fracture mechanism and indicate that cracks should be more difficult to initiate and propagate in the copper than the silver infiltrated material. The higher room temperature strength of copper and the better adherence of the copper/tungsten boundaries support the measured superiority of the copper.

Both of these infiltrant metals display thermal coefficients of expansion that are approximately four times larger than that of tungsten. In the first few seconds of a firing test when the outer tensile stresses are rising rapidly, it would seem that this disparity in the thermal expansion of the infiltrant and the load bearing tungsten structure should aggravate the condition leading to thermal cracking. The volume change of the infiltrant may impose an additional tensile stress on the tungsten skeleton. Thus the fact that the thermal coefficient of silver is approximately 20% larger than that of copper may also contribute to the greater susceptibility to thermal cracking displayed by this material.

ACKNOWLEDGMENT

The assistance of Mr. C. D. Carpenter in preparing the electron micrographs is gratefully acknowledged.

UNCLASSIFIED

U.S. Naval Research Laboratory. Report 6005.
THERMAL SHOCK EVALUATION OF REFRACTORY MATERIALS AS ROCKET NOZZLE INSERTS by E. W. Kammer, H. Smith, and E. Olcott. 51 pp. and figs., November 30, 1963.

Uninfiltrated sintered tungsten of several densities together with copper or silver infiltrated material used as rocket nozzle inserts were examined using a small scale nozzle but with operational temperature, pressure, and time duration of exposure. The nozzle insert walls were notched in a manner to produce stress raisers and their effects on the fracture patterns established relative ratings for resistance to thermal shock. Room temperature fracture toughness factors were also determined from notched bars of these same materials. This toughness factor served as a quality rating score to order the materials in their ability to resist fracture. It was found that copper infiltrated sintered tungsten rated highest on both the model test and on the fracture toughness scale. Mechanical strain

UNCLASSIFIED (over)

1. Refractory materials—Mech. prop.
2. Refractory materials—Thermodyn. prop.
3. Rocket motor nozzles—Materials

I. Kammer, E. W.
II. Smith, H.
III. Olcott, E.

UNCLASSIFIED

U.S. Naval Research Laboratory. Report 6005.
THERMAL SHOCK EVALUATION OF REFRACTORY MATERIALS AS ROCKET NOZZLE INSERTS by E. W. Kammer, H. Smith, and E. Olcott. 51 pp. and figs., November 30, 1963.

Uninfiltrated sintered tungsten of several densities together with copper or silver infiltrated material used as rocket nozzle inserts were examined using a small scale nozzle but with operational temperature, pressure, and time duration of exposure. The nozzle insert walls were notched in a manner to produce stress raisers and their effects on the fracture patterns established relative ratings for resistance to thermal shock. Room temperature fracture toughness factors were also determined from notched bars of these same materials. This toughness factor served as a quality rating score to order the materials in their ability to resist fracture. It was found that copper infiltrated sintered tungsten rated highest on both the model test and on the fracture toughness scale. Mechanical strain

UNCLASSIFIED (over)

1. Refractory materials—Mech. prop.
2. Refractory materials—Thermodyn. prop.
3. Rocket motor nozzles—Materials

I. Kammer, E. W.
II. Smith, H.
III. Olcott, E.

UNCLASSIFIED

U.S. Naval Research Laboratory. Report 6005.
THERMAL SHOCK EVALUATION OF REFRACTORY MATERIALS AS ROCKET NOZZLE INSERTS by E. W. Kammer, H. Smith, and E. Olcott. 51 pp. and figs., November 30, 1963.

Uninfiltrated sintered tungsten of several densities together with copper or silver infiltrated material used as rocket nozzle inserts were examined using a small scale nozzle but with operational temperature, pressure, and time duration of exposure. The nozzle insert walls were notched in a manner to produce stress raisers and their effects on the fracture patterns established relative ratings for resistance to thermal shock. Room temperature fracture toughness factors were also determined from notched bars of these same materials. This toughness factor served as a quality rating score to order the materials in their ability to resist fracture. It was found that copper infiltrated sintered tungsten rated highest on both the model test and on the fracture toughness scale. Mechanical strain

UNCLASSIFIED (over)

1. Refractory materials—Mech. prop.
2. Refractory materials—Thermodyn. prop.
3. Rocket motor nozzles—Materials

I. Kammer, E. W.
II. Smith, H.
III. Olcott, E.

UNCLASSIFIED

U.S. Naval Research Laboratory. Report 6005.
THERMAL SHOCK EVALUATION OF REFRACTORY MATERIALS AS ROCKET NOZZLE INSERTS by E. W. Kammer, H. Smith, and E. Olcott. 51 pp. and figs., November 30, 1963.

Uninfiltrated sintered tungsten of several densities together with copper or silver infiltrated material used as rocket nozzle inserts were examined using a small scale nozzle but with operational temperature, pressure, and time duration of exposure. The nozzle insert walls were notched in a manner to produce stress raisers and their effects on the fracture patterns established relative ratings for resistance to thermal shock. Room temperature fracture toughness factors were also determined from notched bars of these same materials. This toughness factor served as a quality rating score to order the materials in their ability to resist fracture. It was found that copper infiltrated sintered tungsten rated highest on both the model test and on the fracture toughness scale. Mechanical strain

UNCLASSIFIED (over)

1. Refractory materials—Mech. prop.
2. Refractory materials—Thermodyn. prop.
3. Rocket motor nozzles—Materials

I. Kammer, E. W.
II. Smith, H.
III. Olcott, E.

induced in the outer surface of the nozzle insert by temperature gradients across the wall at the beginning of the ignition sequence together with the temperature were measured with the aid of several types of electrical resistance gages. These gages verified that cracking of the nozzle insert wall occurred early in the burning process.

UNCLASSIFIED

UNCLASSIFIED

induced in the outer surface of the nozzle insert by temperature gradients across the wall at the beginning of the ignition sequence together with the temperature were measured with the aid of several types of electrical resistance gages. These gages verified that cracking of the nozzle insert wall occurred early in the burning process.

UNCLASSIFIED

UNCLASSIFIED

induced in the outer surface of the nozzle insert by temperature gradients across the wall at the beginning of the ignition sequence together with the temperature were measured with the aid of several types of electrical resistance gages. These gages verified that cracking of the nozzle insert wall occurred early in the burning process.

UNCLASSIFIED